Study of Electron Identification Capability of the ALICE Transition Radiation Detector

A Dissertation for Master of Science

Department of Physics, Graduate School of Science, University of Tokyo
35-26044 Taku Gunji

Contents

List of Figures viii

List of Tables ix

1 Introduction 1
- 1.1 Ultra-relativistic heavy ion collisions . . . 1
- 1.2 ALICE experiment . . . 1
- 1.3 ALICE Detector Setup . . . 1
- 1.4 TRD at the ALICE experiment . . . 3
- 1.5 The focus of this thesis . . . 3

2 ALICE Transition Radiation Detector 5
- 2.1 Purpose of the ALICE TRD . . . 5
- 2.2 Requirement of the ALICE TRD . . . 6
- 2.3 Transition Radiation . . . 6
- 2.4 Detector Design . . . 9
  - 2.4.1 Radiator . . . 9
  - 2.4.2 Detector . . . 11

3 Test Experiment at CERN 13
- 3.1 Prototype TRD . . . 13
- 3.2 Measurement . . . 15
  - 3.2.1 Beam specification . . . 15
  - 3.2.2 Measurement setup and items . . . 15
  - 3.2.3 Gas conditions . . . 16
- 3.3 Response of the prototype TRDs . . . 17

4 Analysis of the electron identification performance 23
- 4.1 Definition of pion rejection factor . . . 23
- 4.2 Data sample and Event selection . . . 24
  - 4.2.1 Event selection . . . 24
- 4.3 Run Summary . . . 27
- 4.4 Contaminations of data sample . . . 27
- 4.5 Analysis Method-Likelihood ratio method . . . 30

4.5.1 Definition of Likelihood ratio 30
4.5.2 Radiator dependence of pion rejection 30
4.6 Analysis Method-Neural Network method 41
4.7 Incident angle dependence 54
4.8 Magnetic field dependence 56

5 Conclusion **61**

Acknowledgment **63**

A Theoretical description of Transition Radiation **65**
A.1 Single interface 65
A.2 Multiple interface 66

B Drift electrons in the Magnetic field **67**

Bibliohgraphy **69**

List of Figures

1.1 ALICE Detector setup 2
1.2 Cut thought the TRD geometry 4

2.1 Momentum dependence of the number of produced TR photons for electrons (red),muons (light blue), pions(dark blue) and kaons(green) 8
2.2 TR spectrum for single interface (blue) and single foil (red) configurations . . . 8
2.3 the current design of the TRD radiator configuration 10
2.4 the image of fiber mat 10
2.5 the image of PMI form sheets 10
2.6 schematic view of drift chamber. Left panel: geometry of the drift chamber. Right panel: principle of track reconstruction. 11

3.1 The front side of the prototype TRD. Radiator is not attached on the electrode. 14
3.2 The back side view of the prototype TRD. PASA is mounted on the external side of the prototype TRD. 14
3.3 Experimental setup for momentum scan and incident angle scan. 15
3.4 Experimental setup for the measurement in the magnetic field 16
3.5 Experimental setup for the measurement of TR spectrum 16
3.6 Normalized distributions of total energy deposit for pions (left) and electrons (right) at p=4 GeV/c for all chambers. 17
3.7 Pulse height as a function of drift time for pions and electrons. Left panel shows a signal for one event of electron (solid line) and pion (dashed line). Right panel shows mean pulse height distributions for electrons (circle) and pions (square). Open and closed circle (square) is the pulse heights with radiator and without radiator for electrons (pions), respectively 18
3.8 The normalized distribution of energy deposit in TRD in case of pions (left panel) and electrons (right panel). Beam momentum is 4 GeV/c. Solid line is the spectrum taken with radiator and dashed line is the spectrum taken without radiator. 18
3.9 the ratio of most probable value of electron energy deposit to that of pion energy deposit as a function of beam momentum. The results are shown in case of radiator INV6, INV8, AIK6 and PP and in case of no radiator. 19

3.10 Mean relative electron/pion pulse heights as a function of drift region for all radiators. Left and right panel is in case of beam momentum of 3 GeV/c and 6 GeV/c, respectively. 19
3.11 The distributions of energy deposit in different position. 21

4.1 Correlation of the response between one Cherenkov detector and a lead-glass calorimeter for all momenta. 25
4.2 The distribution of each detector after cuts were applied. Beam momentum was 4 GeV/c. Left panel shows the distribution of Cherenkov1 after cuts were done by Cherenkov2 and a lead-glass calorimeter. Central panel shows the distribution of Cherenkov2 after Cherenkov 1 and a lead-glass calorimeter cuts were applied. The right panel shows the lead-glass distribution after two Cherenkov cuts were applied. Red (blue) line is the electron (pion) candidates after cuts being applied by the other two detectors. 26
4.3 The distribution of hit position summed up for each 50 μs. The hit position was defined to be the pad number where maximum pulse height was measured. Yellow region is accept region which indicates that the events whose hit position belongs to the pad number from "1" to "6" are used in this analysis. 26
4.4 Pion probability distribution with pion spectrum (Left) and the electron probability distribution with electron spectrum (Right). Green line is the fitting results. In right panel, solid black line corresponds to the convolution of energy loss and absorption of TR, while dashed black line corresponds to only energy loss. 31
4.5 Likelihood distribution for electrons and pions in case of 1, 2, 3, 4 TRD layers. The arrow indicates the region where the electron detection efficiency is 90%. Radiator is INV8 and beam momentum is 1.54 GeV/c. 32
4.6 Pion misidentification probability as a function of number of TRD layers. Circle means the measured value and triangle means the extrapolated value. 33
4.7 pion rejection factor as a function of momentum extrapolated to 6 TRD layers at electron efficiency of 90%. 33
4.8 The probability distribution of the arrival time of largest cluster generated in the drift region of TRD1. Solid line is that for electrons and dashed line is that for pions. 34
4.9 Likelihood distribution for electrons and pions in case of 1, 2, 3, 4 TRD layers. The arrow indicates the region where the electron detection efficiency is 90%. Radiator is INV8 and beam momentum is 1.5 GeV/c. 35
4.10 Pion misidentification probability as a function of number of TRD layers. Circle means the measured value and triangle means the extrapolated value. 36
4.11 Pion rejection factor based on LQX method as a function of beam momentum. The pion rejection factor is extrapolated to 6 TRD layers at electron efficiency of 90%. 36
4.12 The divided drift region. The energy deposit in the drift region from T0 to T6 were used for 2DLQ analysis. 37

4.13 The deposit energy distribution's for electrons and pions in the sixth drift region at 1.5 GeV/c. Smooth lines are fitting results,, where fitting function is defined in eq. 4.9. 38
4.14 Likelihood distribution for electrons and pions in case of 1, 2, 3, 4 TRD layers based on 2DLQ method. The arrow indicates the region where the electron detection efficiency is 90%. Radiator is INV8 and beam momentum is 1.5 GeV/c. 39
4.15 Pion misidentification probability as a function of number of TRD layers. Circle means the measured value and triangle means the extrapolated value. 40
4.16 Pion rejection factor based on 2DLQ method as a function of beam momentum. The pion rejection factor is extrapolated to 6 TRD layers at electron efficiency of 90%. 40
4.17 The structure of multi-layered feed forward network applied in the analyis. . . . 42
4.18 Electron excite unit output distributions when data sample were transfered 10 times (left panel) and 1000 times (right panel). 44
4.19 Efficiency as a function of learning cycle. Solid and dashed lines are efficiency for learning data and test data, respectively. 45
4.20 Mean error evolution for learning data (solid lines) and test data (dashed lines) as a function of number of learning cycle. 45
4.21 The output distributions of electron excite unit for learning data. Upper left figure is the distribution for 1 TRD layer. Upper right figure is the distribution for 2 TRD layers. Lower left figure is the distribution for 3 TRD layers. Lower right is that for 4 TRD layers. Radiator is INV8 and beam momentum is 1.5 GeV/c. 46
4.22 The input patterns of pulse heights for various electron excite unit output range. Left and Right panel are the input patterns for electrons and pions, respectively. Open circle, open square and open triangle correspond to the output range from 0.8 to 1.0, from 0.5 to 0.8 and from 0 to 0.5, respectively. 47
4.23 correlation between electron excite unit outputs and likelihood ratio for electron events (left panel) and pion events (right panel). 47
4.24 The output distributions of electron excite unit for test data. Upper left figure is the distribution for 1 TRD layer. Upper right figure is the distribution for 2 TRD layers. Lower left figure is the distribution for 3 TRD layers. Lower right is for 4 TRD layers 48
4.25 Pion misidentification probability as a function of number of TRD layers. Circle means the measured value and triangle means the extrapolated value. 49
4.26 Pion rejection factor based on neural network as a function of beam momentum. 49
4.27 The energy deposit distributions of each drift region. Shaded areas are the spectra of misidentified pions, red lines and blue lines are electron spectra and pion spectra, respectively. The beam momentum is 2 GeV/c. 51
4.28 The number of electrons liberated per unit cm with the energy more than E in Xe gas [32]. 52

4.29 Simulated energy loss of 2 GeV/c pions in the TRD. Solid line is the energy loss for all tracks, dashed line is that for the tracks which do not have any δ electrons, dotted line is that for tracks with δ electrons which do not escape from the detector and dot-dashed line is that for tracks which δ electrons escape from the detector. 53
4.30 Read data of energy loss of 2 GeV/c pions in the TRD. 53
4.31 Average pulse height as a function of drift time, for different incident angles. Left panel: electrons, right panel: pions. 54
4.32 Left panel: Average pulse heights ratios as a function of drift region. Central panel: Average pulse heights ratios of electrons to those of electrons at 0 deg. Right panel: Average pulse heights ratios of pions to those of pions at 0 deg. . . 54
4.33 Pion rejection factor as a function of incident angle. Radiator is INV6 and beam momentum is 3 GeV/c. 56
4.34 Pulse heights distributions for electrons (left) and pions (right) as a function of drift time for different magnetic fields 57
4.35 Average relative electron/pion pulse heights as a function of drift region for various magnetic fields. Radiator is INV6 and beam momentum is 6 GeV/c. . . 57
4.36 Pion rejection factor as a function of magnetic field. 59

B.1 The drift path of electrons without magnetic field (left) and with magnetic field (right). 68

List of Tables

1.1 Overview of specifications of ALICE TRD 4

2.1 The properties of the radiator materials 9
2.2 The specifications of the readout chamber. 12

3.1 The properties of four radiators tested at this experiment 14
3.2 The properties of secondary beam at T10 beam line 15
3.3 The definition of drift region. 20

4.1 Threshold values for event selection of electrons and pions 24
4.2 Summary of run information to be used to study radiator dependence of electron identification capability. 28
4.3 Summary of run information to be used to study incident angle dependence of electron identification capability. In case of incident angle of 0 degree, the calorimeter wasn't in good operation and the calorimeter wasn't used to separate between electron events and pion events. 29
4.4 Summary of run information to be used to magnetic field dependence of electron identification capability. Since the trigger reduction wasn't applied, there were small number of electron events. 29
4.5 contamination for all momenta. 29
4.6 Comparison of the results of pion rejection factor at 6 TRD layers based on LQ method, LQX method and 2DLQ method. 41
4.7 Comparison of pion misidentification probability as a function of number of TRD layers extracted for learning data based on neural network method and 2DLQ method. Radiator is INV8 and beam momentum is 1.5 GeV/c. 46
4.8 Comparison of pion rejection factor based on neural network and 2DLQ method. 50
4.9 Lorentz angle for different magnetic fields of the test experiment. 58

Chapter 1

Introduction

1.1 Ultra-relativistic heavy ion collisions

The purpose of the relativistic heavy ion collision experiments is to realize strongly interacting matter at extremely high energy densities and to study its various properties. Lattice QCD calculations predict that, at the high energy density, there will be a phase transition from ordinary hadronic matter to a plasma of deconfined quarks and gluons, called Quark-Gluon-Plasma (QGP). Relativistic heavy ion collisions enable us to understand the fundamental questions of confinement, chiral-symmetry breaking and the nature of QCD phase transition. Moreover, since QGP phase is believed to have existed in the early universe during a few microseconds after the Big Bang, relativistic heavy ion collisions also shed light on the field of astronomy and cosmology.

1.2 ALICE experiment

The ALICE experiment (A Large Ion Collider Experiment) [1] is one of the experiments at the Large Hadron Collider (LHC) at CERN. The ALICE experiment will start its operation in 2007. The ALICE experiment is dedicated to study the properties of extreme hot and dense matter in high energy heavy ion collisions at $\sqrt{s_{NN}} = 5.5$ TeV, which is $\sim$30 times larger than that of the Relativistic Heavy Ion Collider (RHIC) at Brookhaven National Laboratory (BNL).

1.3 ALICE Detector Setup

There are many signatures of QGP having been proposed so far [2]. However, any of them cannot be taken solely as the signature because of large ambiguity. Therefore the ALICE detector is designed to measure a large set of observables over as much of phase space as achievable. The ALICE experimental setup is shown in the Figure 1.1.

The main components of the ALICE detector will be constructed in the central barrel region, covering pseudorapidity range $-0.9 \leq \eta \leq 0.9$ with full azimuthal coverage, where the pseudorapidity, η, is defined as $\eta = -\ln(\tan\frac{\theta}{2})$ and θ is the angle between the particle momen-

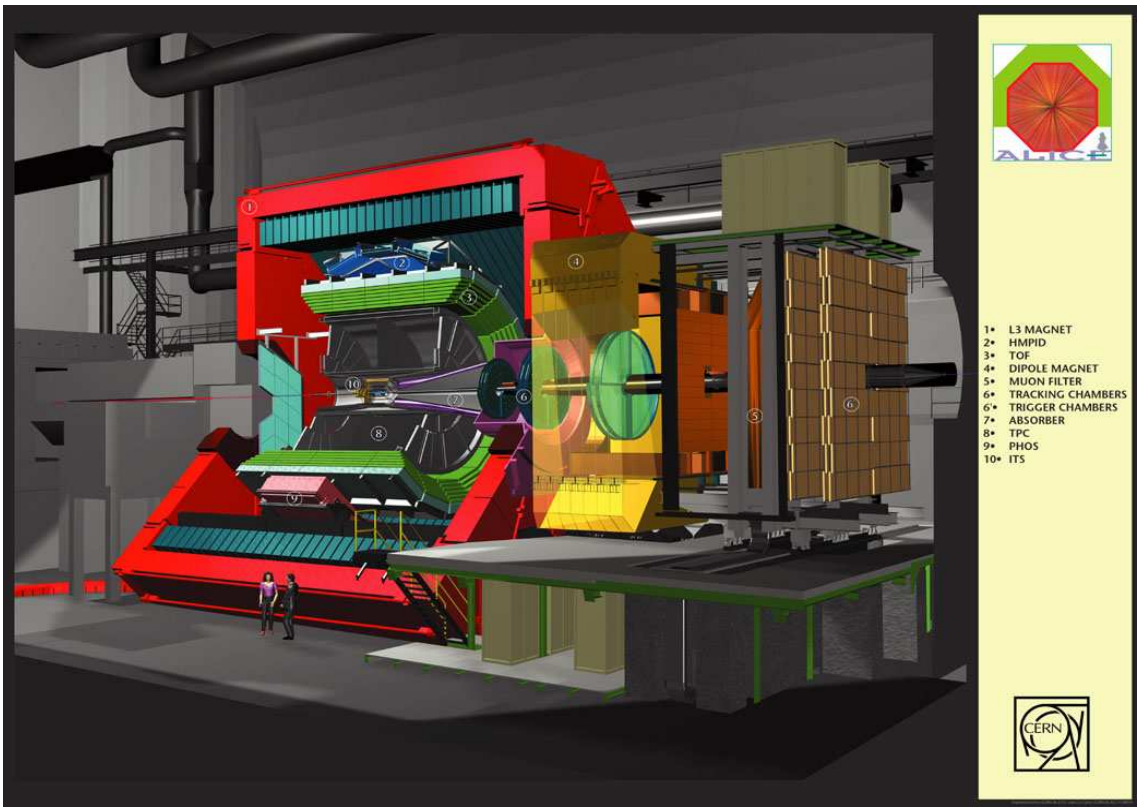

Figure 1.1: ALICE Detector setup

tum vector and the beam axis. The central barrel is contained in the L3 magnet (B=0.4 T) and consists of an inner tracking system of Silicon detectors (ITS) [1], a large time projection chamber (TPC) [1], which are the main devices for tracking of charged particles, a transition radiation detector (TRD) [3, 4] for electron identification and track reconstruction of charged particles and a time-of-flight array (TOF) [1] for particle identification. In addition, there will be two single arm detectors at the mid-rapidity, an array of ring-imaging Cherenkov counters (HMPID) for identification of high momentum hadrons and a photon spectrometer (PHOS) to detect photons. At the pseudorapidity range $2.5 \leq \eta \leq 4.0$, a muon spectrometer will be installed with its own dipole magnet. At more forward and backward rapidity range, there will be detectors to measure the multiplicity of charged particles and the time of interaction and to provide triggers.

1.4 TRD at the ALICE experiment

ALICE TRD is briefly described in this section. Its details concerning on the current design of the ALICE TRD and the prototype TRD are described in chapter 2 and chapter 3.

The coverage in peudorapidity matches the coverage of the TPC ($|\eta| \leq 0.9$). In radius direction, the TRD fills the space between TPC and TOF as shown in Fig. 1.1. The TRD consists of 6 individual layers for sufficient capability of electron identification.

In each layer, there are 18 sectors along the azimuthal angle and 5 sectors along the beam direction as shown in Fig. 1.2. Therefore the total number of TRD segments are $18 \times 5 \times 6 = 540$ segments. Each segment consists of radiator of 4.8 cm thickness, a readout chamber and the front-end electronics mounted on the readout chamber. Each chamber has 144 readout pads in azimuthal direction and between 12 and 16 pad rows in the beam direction. The pads have a typical size of 6-7 cm^2 and cover a total area of 736 m^2 with 1.16×10^6 readout channels. The gas mixture in the readout chamber is Xe(85%) and CO_2(15%). Each readout chamber has a drift region of 3.0 cm and an amplification region of 0.7 cm. The drift time in the drift region is 2.0 μs with the drift velocity of 1.5 cm/μs. This drift velocity will be reached with the electric field of 0.7 keV/cm. In this gas mixture, the gas gain will reach order of 5×10^3. Table 1.1 is the summary of the parameters concerning on the ALICE TRD.

1.5 The focus of this thesis

The ALICE TRD is the main device of electron identification and track reconstruction of charged particles. In this thesis, the capability of electron identification of the prototype TRD [19, 20] is a central topic and has been studied by using various analysis methods. In next chapter, the properties of transition radiation and current design of the ALICE TRD are described. In chaper 3, the prototype TRD, test experiment which was held on 2002 at CERN and responses of prototype TRDs are described. In chapter 4, analysis methods to be utilized for the study of electron identification capability and the analysis results are described. The conclusion is summarized in chapter 5.

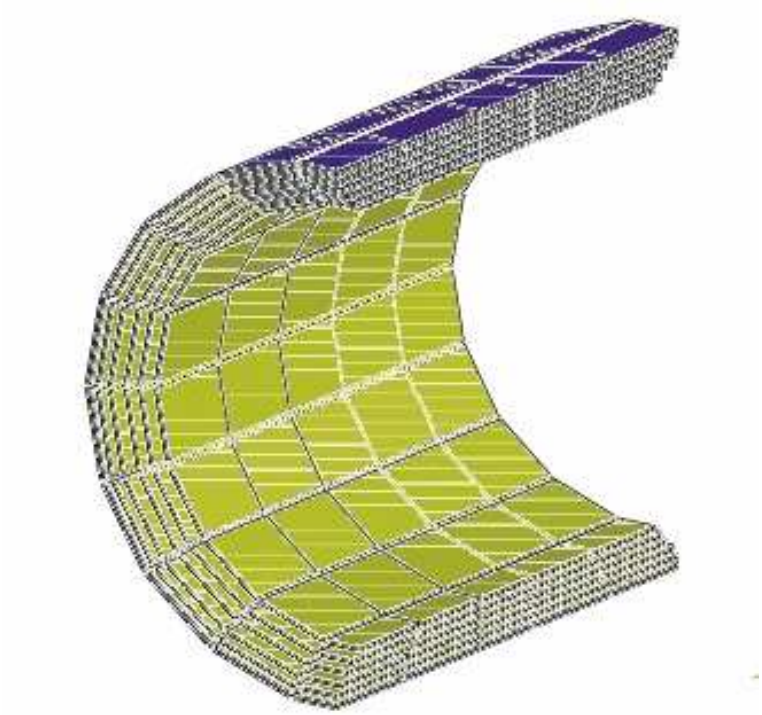

Figure 1.2: Cut thought the TRD geometry

Table 1.1: Overview of specifications of ALICE TRD

Psedorapidity coverage	$-0.9 \leq \eta \leq 0.9$
Azimuthal coverage	2π
Radial position	$2.9 \leq r \leq 3.7$ m
Length	maximum 7.0 mm
Segments in azimuthal direction	18
Segments in beam direction	5
Segments in radial direction	6 layers
Total number of TRD segments	540
Largest segment size	120×159 cm^2
Detector active area	736 m^2
Detector thickness radially	$X/X_0 = 14.3$ %
Radiator	fibers+foam sandwich, 4.8 cm per layer
Number of pads in azimuthal direction	144
Number of pad rows in beam direction	12-16
Typical pad size	0.725×8.75 cm^2
Number of readout channels	1.16×10^6

Chapter 2

ALICE Transition Radiation Detector

In this chapter, details of the ALICE Transition Radiation Detector [3] are described.

2.1 Purpose of the ALICE TRD

The purpose to install the TRD is to identify electrons and reconstruct tracks of charged particles. The capability of electron identification is worse at momentum above 3 GeV/c by measuring energy loss in the TPC, where the rejection factor is below 100 at the momentum above 3 GeV/c. The addition of the TRD to the central ALICE barrel will provide the rejection factor in the order of hundred and sufficient electron identification. This capability makes it possible to measure following observables in conjunction with the information from TPC and ITS [3, 4].

- di-electron channel:
  production of heavy vector-meson resonances as well as the di-lepton continuum.

- single-electron channel:
  the semi-leptonic decays of hadrons with open charm and open beauty.

- coincidences of electrons and muons:
  information on the correlated production of hadrons with open charm and open beauty.

From these observables, the following physics can be addressed [4].

- Spectroscopy of heavy and light vector meson resonances

- Measurement of the open charm and open beauty cross sections

- Identification of J/ψ mesons from B decay. This is a serious background for the measurement of "direct" J/ψ.

- Access to the dilepton continuum at the Drell-Yan level.

J/ψ measurement is one of the probes to inspect the QGP formation because it is predicted that the J/ψ yield is suppressed by the dissociation due to Color Debye screening effect in QGP [5]. On the other hand, recent theoretical models predict the enhancement of J/ψ yield at LHC energy [6, 7]. To determine the scenario concerning on the J/ψ production, it is of great importance to extract J/ψ yield by measuring J/ψ decay to e^+e^- at central region.

2.2 Requirement of the ALICE TRD

Requirements can be summarized as follows.

- Pion rejection capability
  J/ψ measurement at wide range of transverse momentum, p_T, is a decision factor to the pion rejection capability. Pion rejection factor of 100 at electron detection efficiency of 90% is the design goal of the ALICE TRD.

- Position resolution and angular resolution
  A good position resolution and angular resolution are required for an efficient and unambiguous matching of tracks reconstructed in the TPC. A good position resolution and angular resolution would be essential for a good momentum resolution. A momentum resolution affects the mass resolution of J/ψ and Υ. Moreover, a good momentum resolution is important since TRD will be used as a trigger device. The TRD trigger on high momentum electrons will be used to increase statistics for the J/ψ and Υ measurements. The TRD will provide a momentum resolution of 5% at 5 GeV leading the accuracy of the point reconstruction of 30% of the pad width.

- The thickness of the TRD
  The thickness of the TRD in radiation lengths has to be kept as small as possible to avoid the production of fake tracks.

- The granularity
  In order to cope with the huge particle multiplicities, which are expected to be as high as 8000 charged hadrons per unit rapidity for Pb-Pb collisions at maximum LHC energy, a high granularity is necessary. The granularity is driven in bend direction by the required momentum resolution and along the beam direction by the required capability to identify electron tracks efficiently. The readout pads of about 6 cm^2 are designed for the tracking efficiency to be achieved more than 80%.

2.3 Transition Radiation

Transition Radiation (TR) was first predicted by Ginzburg and Frank in 1946 [8] and its characteristics have been long studied both theoretically [9, 10, 11] and experimentally [12, 13, 14]. Consequently, TRDs have been used or now being used in many experiments: NOMAD [15], ZEUS [16], PHENIX [17], ATLAS [18] and so on.

In this section, some important properties of transition radiation are described. Theoretical description of transition radiation is summarized in Appendix A.

TR is emitted when a charged particle with relativistic high momentum moves across the interface of two media with different dielectric constants. The TR yield is proportional to the Lorentz factor, γ, in case of single interface as shown in Eq. A.4. The probability of emitting a TR photon per interface is of the order of the fine structure constant and therefore must be enhanced for the experimental studies. This may be achieved by using a multi-layered structure with many interfaces as a configuration of radiator. However, in case of the radiator configuration of multi-layered structure, the interface effects occur and the TR yield is suppressed as described in Appendix A. This interface effects are interpreted in terms of "formation zone". Now assuming that the radiator is composed of a stack of N_f foils of thickness l_1 separated by a medium of thickness l_2, the "formation zones" for two media are defined as follows:

$$Z_i \equiv \frac{4}{\omega}\Big(\frac{1}{\gamma^2} + \theta^2 + \frac{\omega_i^2}{\omega^2}\Big)^{-1} \tag{2.1}$$

The double differential energy spectrum is written in terms of "formation zone" as follows:

$$\Big(\frac{\mathrm{d}^2\mathrm{W}}{\mathrm{d}\omega\mathrm{d}\Omega}\Big)_{stack} = \Big(\frac{\mathrm{d}^2\mathrm{W}}{\mathrm{d}\omega\mathrm{d}\Omega}\Big)_{interface} \times 4\sin^2\Big(\frac{l_1}{Z_1}\Big) \times \exp\Big(\frac{1-N_f}{2}\sigma\Big)\frac{\sin^2(N_f\phi_{12}/2) + \sinh^2(N_f\sigma/4)}{\sin^2(\phi_{12}/2) + \sinh^2(\sigma/4)} \tag{2.2}$$

where $\Big(\frac{\mathrm{d}^2\mathrm{W}}{\mathrm{d}\omega\mathrm{d}\Omega}\Big)_{interface}$ is described as Eq. A.1, $\phi_{12} = \phi_1 + \phi_2$ is phase retardation as defined in Eq. A.6 and $\sigma = \sigma_1 + \sigma_2$ is the total absorption cross section. If $l_i \ll Z_i$, the TR yield is suppressed. This is the "formation zone" effect.

Since the "formation zone" is approximately proportional to γ^2, the production mechanism and the suppression effect contribute to the saturation of TR yield for a particle with higher Lorentz factor. The number of emitted TR photons is approximately proportional to the Lorentz factor of the particle but the interface effect as described above causes the saturation of number of emitted TR photons as the Lorentz factor becomes larger. Figure 2.1 shows the number of emitted TR photons for electron (red), muon (light blue), pion (dark blue) and kaon (green) as a function of momentum. The interface effects are taken into account. More than one TR photon can be emitted when the Lorentz factor is more than ~ 2000, which corresponds to electron momentum of about 1 GeV/c and pion momentum of about 280 GeV/c. Therefore from 1 GeV/c to 280 GeV/c, electron can be identified by detecting TR.

Figure 2.2 shows the differential energy spectrum per interface for single interface (blue) and single foil (red) radiator, where the self-absorption is not taken into account. The single interface is the radiator which has only one boundary and differential energy spectrum is described in Eq. A.2, while the single foil is the one which has two boundaries and the double differential energy spectrum is described in Eq. A.8. In case of single foil, there is an osscilation because of "formation zone" effect as described above. The self-absorption in the radiator causes the suppression of the TR yield for the TR photons with lower energies. As a result, the emitted TR photon is soft X-ray and its emission angle is $\sim 1/\gamma$.

The typical energy of emitted TR photons is $\sim$10 keV and number of emitted photons is $\sim$1 for the radiator of the ALICE TRD [1].

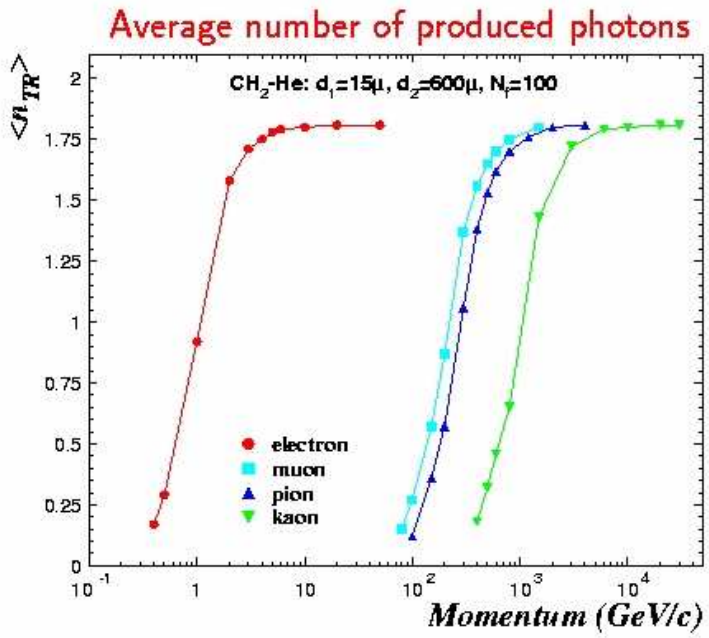

Figure 2.1: Momentum dependence of the number of produced TR photons for electrons (red),muons (light blue), pions(dark blue) and kaons(green)

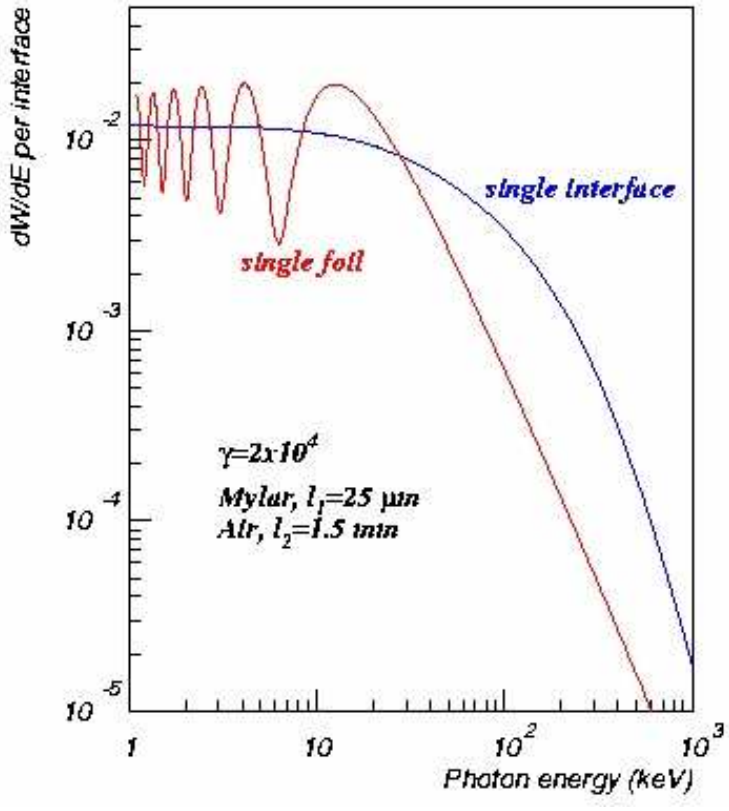

Figure 2.2: TR spectrum for single interface (blue) and single foil (red) configurations

2.4 Detector Design

In this section, detector design is described. The TRD consists of two parts; one is the radiator which generates the TR photons, and the other is the detector part which detects the TR photons. At the current design of the ALICE TRD, the radiator consists of hundreds of fiber mats and the readout chamber is mounted behind radiator to detect TR photons.

2.4.1 Radiator

Since the probability of emitting a TR photon per interface is the order of fine structure constant, radiator needs to have a large number of interfaces. Therefore radiator material may be distributed in layers like a regular stack of foils or in an irregular structure like forms or fibers. The latter have the advantage that they are much easier to handle and to produce. To reduce self-absorption of the emitted TR photon, all materials need to be low atomic number.

Besides the above requirement, the ALICE TRD has to satisfy the geometrical and mechanical constraints. In the ALICE experiment, six TRD layers, each of which has full azimuthal coverage, will be installed. The radiator should not be suffered from the overpressure from gravity. It is difficult to maintain a uniform separation of the foils, since the bending foils under the influence of the gravitational force cannot be neglected. This circumstance excludes the use of regular stacks of foils. Moreover, the radiator is attached to the entrance window of the readout chamber which serves simultaneously as the drift electrode. The radiator itself is intended to support the entrance window of the readout chamber.

The design of the radiator is a compromise between the TR yield and geometrical and mechanical stability as described above. Various radiator materials and types (foils, forms and fibers) were tested at the previous measurements at GSI darmstat* [3, 19, 20]. From these experiments, in conjunction with the requirements explained above, the following radiator design was chosen. Figure 2.3 shows the current design of the configuration of the TRD radiator. The radiator consists of multi-layered media of irregular polypropylene (PP) fibers of diameter 17 μm sandwiched by the polimethacrylimid (PMI) form sheets (Rohacell HF71) of thickness of 8 mm. This PMI sheets cover upper and lower side of the PP fibers and support the entrance window of readout chamber. A carbon fiber sheets of 100 μm thickness is coated on the external sides of these PMI sheets to guarantee a flat surface of the radiator and drift electrode. The properties of these radiator materials are summarized in Table 2.1, and the images of PP fibers and PMI sheets scanned by electron microscope are shown in Fig. 2.4 and Fig. 2.5, respectively.

Table 2.1: The properties of the radiator materials

material	density[g/cm^3]	radiation length X_0 [g/cm^2]	absolute thickness[cm]	X/X_0 [*10^{-3}]
PMI form	0.075	40.6	2*0.8	2.96
PP fiber	0.074	44.6	3.0	5.30

*Gesellschaft für Schwerionenforschung, Plankstr. 1, 64291 Darmstadt, Germany

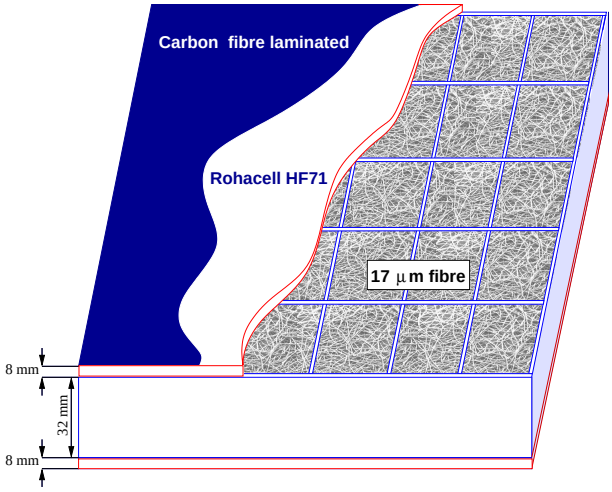

Figure 2.3: the current design of the TRD radiator configuration

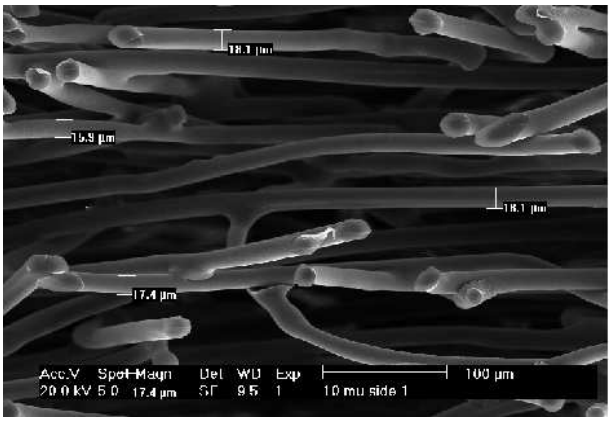

Figure 2.4: the image of fiber mat

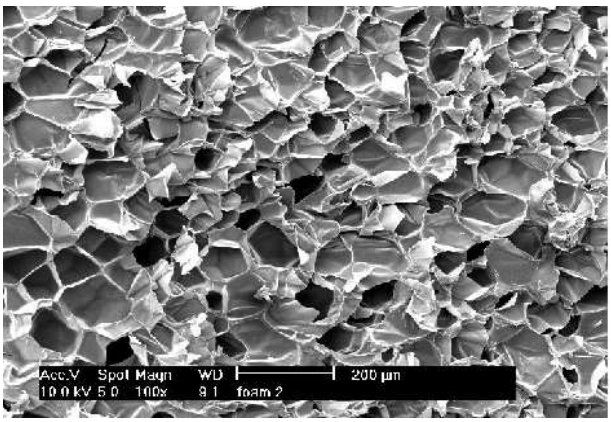

Figure 2.5: the image of PMI form sheets

2.4.2 Detector

To detect TR photons with the energy around 10 keV, the readout detector needs to have high detection efficiency around soft x-ray region. The drift chamber which contains a heavy noble gas is a suitable device for this purpose. Since the absorption length of Xenon is 1 cm for a photon with energy of 10 keV, the current design of the gas components of readout chamber is 85% Xe and 15% CO_2. The CO_2 gas is used as quencher. Most TR photons are absorbed near the entrance window in the drift chamber and about 95% of TR photons are absorbed in the drift region.

The drift chamber has a drift gas volume and a wire amplification region with the cathode pad readout. Figure 2.6 shows the schematic view of the drift chamber of TRD. The drift region

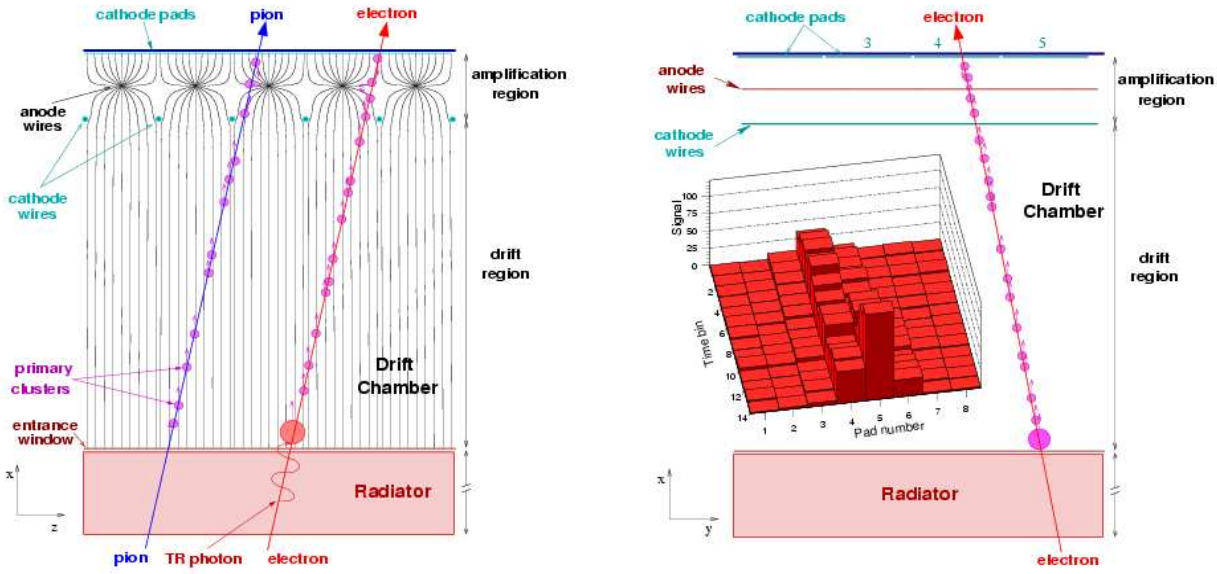

Figure 2.6: schematic view of drift chamber. Left panel: geometry of the drift chamber. Right panel: principle of track reconstruction.

and amplification region are separated by the cathode wire plane. The drift chamber has a drift region of 30 mm and an amplification region of 7 mm. Anode wires (W-Au) of 20 μm diameter are used, with a pitch of 5 mm and are centered between pad plane and cathode wire plane with a gap of 3.5 mm. The cathode wires (Cu-Be) have 75 μm diameter with a pitch of 2.5 mm. The signal is induced on a segmented cathode plane with rectangular pads of $8.0 \times 7.5 = 6.0$ cm^2.

The cathode wires are kept to be the same potential as the pad plane (ground). The anode wires are biased by a positive potential. Electrons produced in the drift volume move towards the cathode wires and start an avalanche close to the anode wires. In the process of avalanche near the anode wires, a cloud of positive ions is created and moves slowly away from the anode wire.

The specifications of the drift chamber is summarized in Table 2.2.

Table 2.2: The specifications of the readout chamber.

Typical pad size	$0.75 \times 8.0 = 6.0$ cm^2
Detector Gas	Xe (85%), CO_2 (15%)
Depth of drift region	3 cm
Depth of amplification region	0.7 cm
Distance between pad plane and anode wire plane	0.35 cm
Distance between anode and cathode wire plane	0.35 cm
Anode wire pitch	5 mm
Cathode wire pitch	2.5 mm
Drift field	0.7 kV/cm
Drift velocity	1.5 cm/μs
Potential at entrance window	-2.1 kV
Potential at cathode wire	0 kV (GND)
Potential at anode wire	1.5 kV
Potential at cathode plane	0 kV (GND)
Gain	order of 5×10^3

Chapter 3

Test Experiment at CERN

Four prototype TRDs were developed based on the earlier measurements [3, 19, 20]. These modules were tested in October 2002 at T10 beam line at CERN PS to determine the final design of the ALICE TRD by studying the electron identification capability and track reconstruction capability. In this chapter, the structure of the prototype TRDs, the measurement setup together with specification of T10 beam line and measurement items are described. Some detector responses are shown at the last section.

3.1 Prototype TRD

The prototype TRD has the same configuration as the current design of the ALICE TRD except for the whole size; the prototype TRD has a small active area (25×32 cm^2). Four radiators were prepared to fix the final design of the radiator. The specifications of these four radiators are summarized in Table 3.1. INV6, INV8 and AIK6 are the multi-layered media of PP fibers sandwiched by the PMI sheets as shown in Fig. 2.3. Pure fiber is also the multi-layered media of PP fibers but not sandwiched by PMI sheets. PMI sheets is coated on only one side of PP fibers. These four radiators were tested to choose the most suitable radiator in terms of TR yield and mechanical stability. INV6 and AIK6 are the same configuration but these is a difference in the manufactures which coated carbon fibers on the external sides of the PMI form sheets.

The signal is induced on the segmented cathode pad and fed into the prototype of the charge-sensitive preamplifier/shaper (PASA). It has a noise of 1000 electrons and shaping time of about 120 ns FWHM. The gain is about 6 mV/fC. The FADC prepared for the test experiment is different from the one designed for the ALICE TRD. It has an 8-bit conversion and adjustable baseline. The sampling frequency was set to be 20 MHz. The data acquisition (DAQ) was based on the MBS system which was developed at GSI [21]. The MBS system is operated with the VME event builder, RIO2 [22]. The FADC modules were connected to the RIO2 by a VSB bus. Since the beam diameter is about 2.5 cm, only eight central pads were connected to the above readout electronics.

Figure 3.1 and Figure 3.2 are the pictures of prototype TRD from the front side and back side, respectively.

Table 3.1: The properties of four radiators tested at this experiment

Radiator Name	Radiator Material	thickness [cm]
INV6	PP fiber	3.6
(sandwich)	PMI form sheets	1.2
	Carbon fiber	0.02
INV8	PP fiber	3.2
(sandwich)	PMI form sheets	1.6
	Carbon fiber	0.02
AIK6	PP fiber	3.6
(sandwich)	PMI form sheets	1.2
	Carbon fiber	0.02
Pure fiber	PP fiber	3.6
(no-sandwich)	PMI form sheets	0.6
	Carbon fiber	0.01

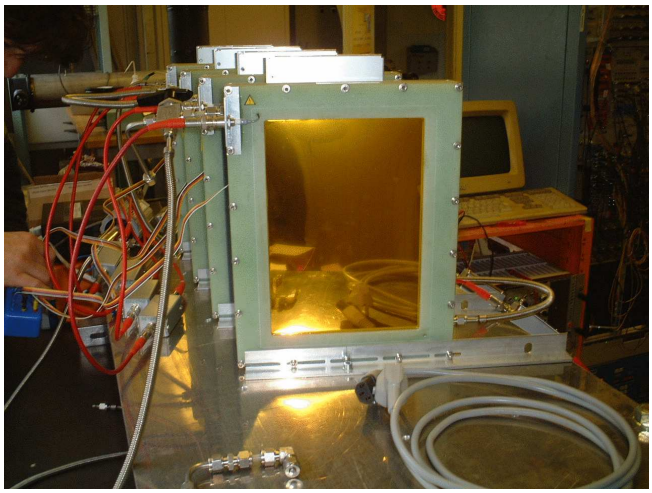

Figure 3.1: The front side of the prototype TRD. Radiator is not attached on the electrode.

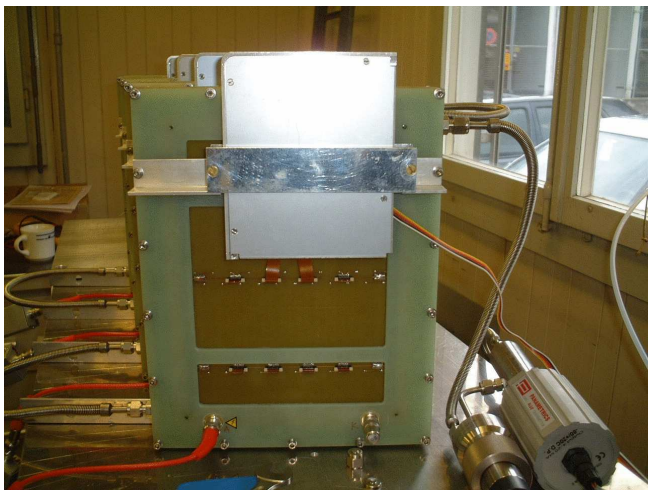

Figure 3.2: The back side view of the prototype TRD. PASA is mounted on the external side of the prototype TRD.

3.2 Measurement

3.2.1 Beam specification

The test experiment was performed at T10 beam line of the Proton Synchrotron at CERN [23]. The primary beam of protons with momentum of 24 GeV/c collides with the internal targets (Al, Cu, Be or ZnS) and the secondary particles, $p^{\pm}$, $\pi^{\pm}$, $K^{\pm}$ and $e^{\pm}$, are created. These secondary particles come to the T10 beam line. The momentum range of the secondary beam is from 0.5 GeV/c to 7 GeV/c. The properties of the secondary beam at T10 beam line is summarized in Table 3.2.

Table 3.2: The properties of secondary beam at T10 beam line

Momentum range	0.5 - 7 GeV/c
Particle ratio of $e^{\pm}/\pi^{\pm}$	50% at 1 GeV/c 1% at 5 GeV/c 0.1% at 7 GeV/c
Beam spread	diameter 2.0 cm at focus point in case of 7 GeV/c
Momentum resolution	3.5% (no collimeter)
Position resolution	1.3 cm in horizontal, 0.55 cm in vertical (no collimator)
incident Angle resolution	3.8 mrad in horizontal, 10.6 mrad in vertical (no collimator)
number of particles per spill	10^6 maximum

3.2.2 Measurement setup and items

The schematic view of the experimental setup is shown in Fig. 3.3. Two air-filled Cherenkov

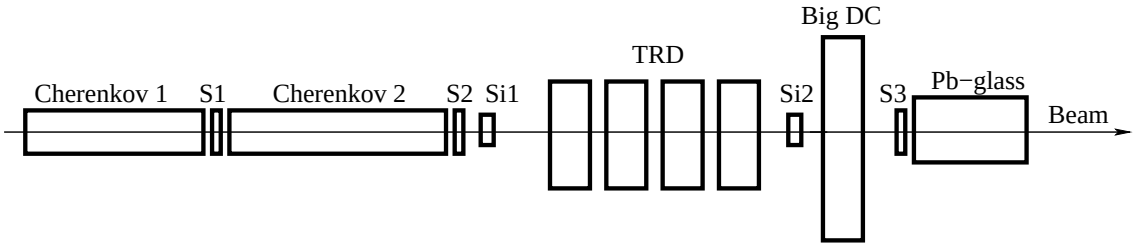

Figure 3.3: Experimental setup for momentum scan and incident angle scan.

counters with 2 m in length and a lead-glass calorimeter with 25 cm in depth, which corresponds to 10 radiation length, were used for the separation of electron events and pion events. Pions with momentum above 4.5 GeV/c emits Cherenkov lights in these two air-filled Cherenkov counters. Three scintillators were used to generate the trigger signal to start data acquisition. The size of these scintillators was 60 mm $\times$ 60 mm and 20 mm in depth. Two silicon strip detectors were used for the measurement of the position of incident particles. Each silicon strip

detector consists of two single sided silicon sensors: one is for horizontal and the other is for vertical position measurement. Each single sided silicon sensor has the effective area of 32 mm $\times$ 32 mm and thickness of 300 μm. The strip pitch is 50 μm and the number of readout strips are 640. The big chamber is the same as the one segment of the ALICE TRD with the radiator material of INV8. However this big chamber was not used in data analysis because of its large noise. Since number of electrons per spill decreases as shown in Table 3.2, the trigger reduction was applied to reduce pion events and to acquire similar sample size of electron and pion events.

The main sets of measurements with using these devices are listed below.

- Momentum scan (1, 1.5, 2, 3, 4, 5, 6 GeV/c) for four radiator types (PP fibers, INV6, INV8, AIK6) and without radiators
- Incident angle scan (0, 5, 10, 15 degrees with respect to nominal to anode wires)
- Measurement in magnetic field ($\pm$0, $\pm$0.14, $\pm$0.28, $\pm$0.42, $\pm$0.56 T)
- Measurement with converter (Al with thickness of 9% X_0)
- Measurement of pure TR spectrum by using beam deflection in magnetic field

The setups for the measurement in the magnetic field and for the measurement to obtain pure TR spectrum are shown in the Figure 3.4 and Figure 3.5, respectively.

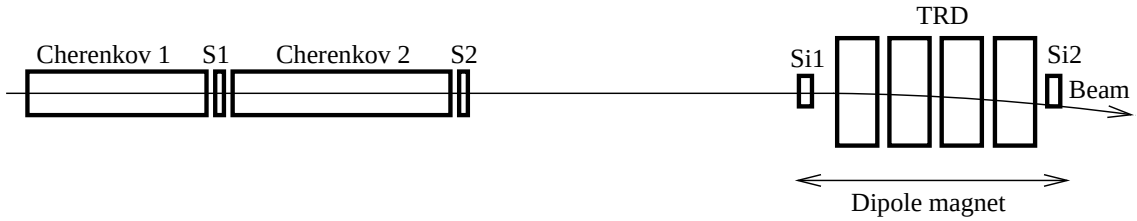

Figure 3.4: Experimental setup for the measurement in the magnetic field

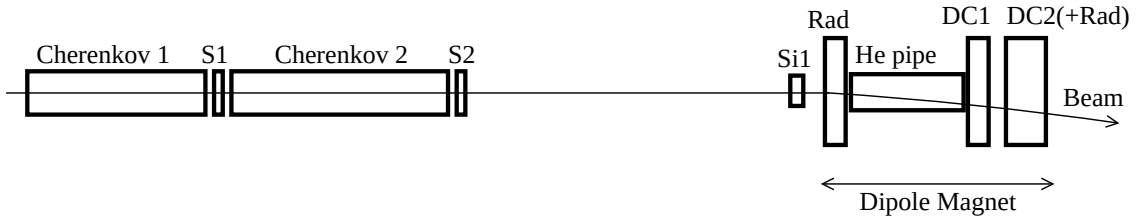

Figure 3.5: Experimental setup for the measurement of TR spectrum

3.2.3 Gas conditions

During the test experiment, the drift chambers were operated with the gas mixture of Xe (85%), CO_2 (15%) at atmospheric pressure. Contaminations with oxygen and water were at the level of 170 ppm and 800 ppm, respectively.

3.3 Response of the prototype TRDs

Figure 3.6 shows the normalized distributions of total energy deposit in each TRD with INV8 radiator. The left panel is for incident pions and the right panel is for electrons. Four prototype

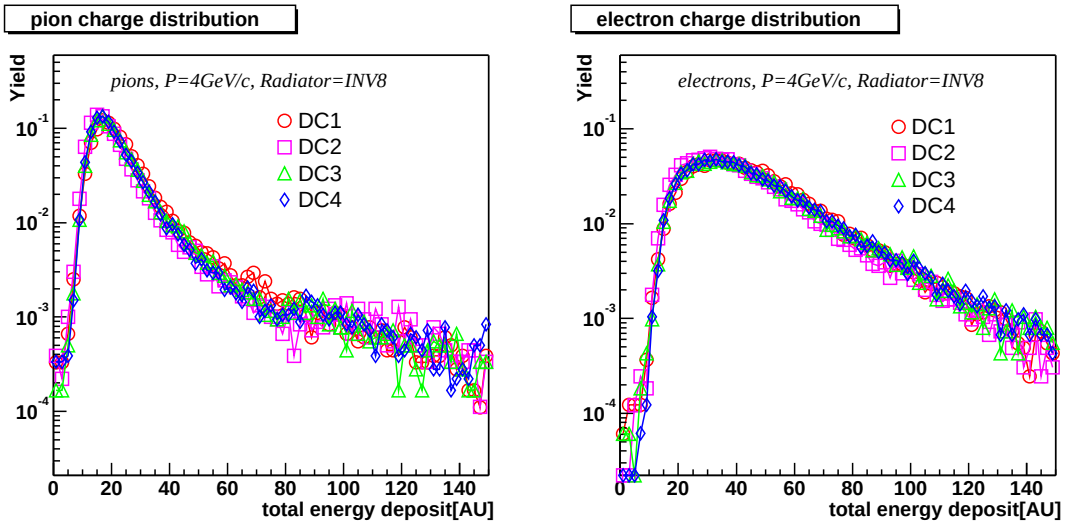

Figure 3.6: Normalized distributions of total energy deposit for pions (left) and electrons (right) at p=4 GeV/c for all chambers.

TRDs show identical responses for electrons and pions.
Figure 3.7 shows the pulse heights for one event (left) and the mean pulse heights for all events (right) as a function of drift time, respectively. In the left panel, solid line is the pulse heights for one electron event and dashed line is those for one pion event. A large spike from X-ray absorption, which is the signature of TR, can be seen around the end of drift time only in electron event. In the right panel, closed circle (square) and open circle (square) are mean pluse heights for electron (pion) events with radiator and without radiator, respectively. For electrons, there is a significant increase in the mean pulse height at later drift time in case of radiator used, while for pions the pulse height distributions are almost the same with radiator and without radiator. The peak at short drift time originates from the primary clusters created in the amplification region, where the ionization from both sides of anode wires contributes to the same time interval. Due to the large electric field of amplification region compared to that of drift region, the drift velocity in the amplification region is larger than that in the drift region.

The comparison of energy deposit distributions with radiator and without radiator are shown in Fig. 3.8. The energy deposit distributions with and without radiator are almost the same for pions. On the other hand, the distributions with and without radiator is greatly different for electrons. Since the transition radiation photon is absorbed in the TRD in case of electron events, the mean value and the most probable value of the distributions with radiator are larger than those without radiator.

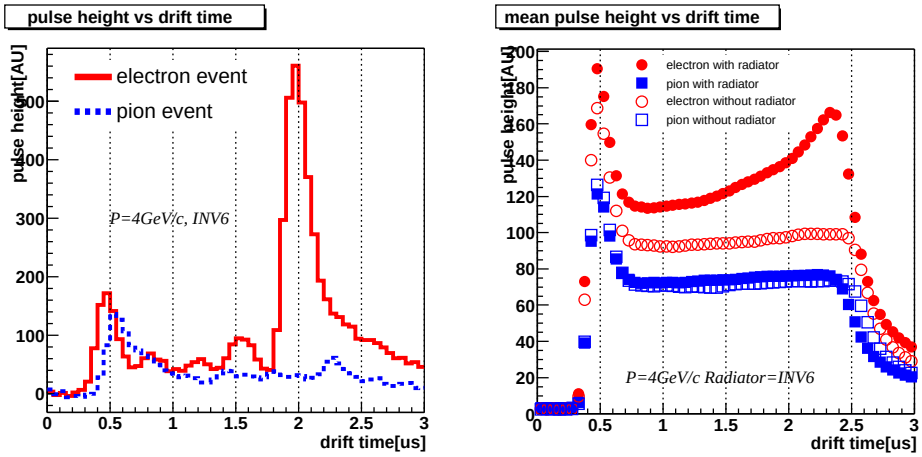

Figure 3.7: Pulse height as a function of drift time for pions and electrons. Left panel shows a signal for one event of electron (solid line) and pion (dashed line). Right panel shows mean pulse height distributions for electrons (circle) and pions (square). Open and closed circle (square) is the pulse heights with radiator and without radiator for electrons (pions), respectively

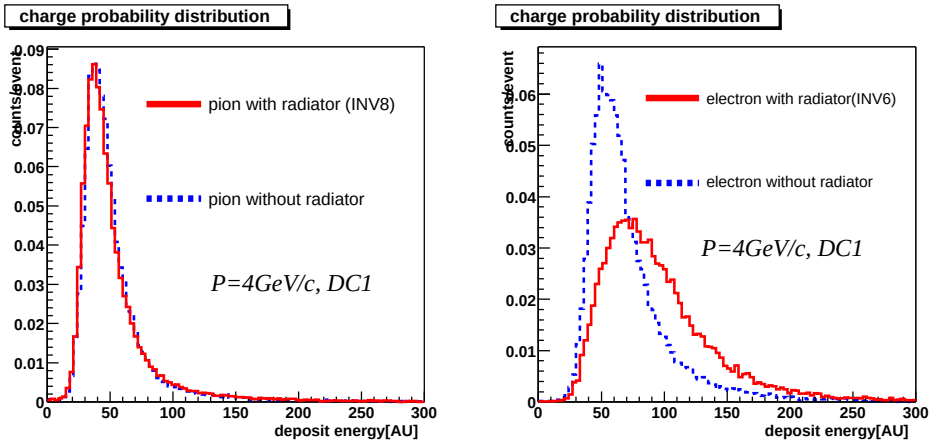

Figure 3.8: The normalized distribution of energy deposit in TRD in case of pions (left panel) and electrons (right panel). Beam momentum is 4 GeV/c. Solid line is the spectrum taken with radiator and dashed line is the spectrum taken without radiator.

Figure 3.9 shows the ratio of the most probable value of energy deposit for electrons to that for pions as a function of momentum. Energy loss of pions becomes larger as the pion momentum is larger than 1.0 GeV/c, while the energy loss of electrons is constant for more than 1.0 GeV/c. This is reflected in the momentum dependence of the ratio in case of without radiator as shown in Fig. 3.9. The ratios for sandwich type radiators (INV6, INV8 and AIK6) are smaller than that for the PP fibers because of the self-absorption of TR photons in PMI sheets.

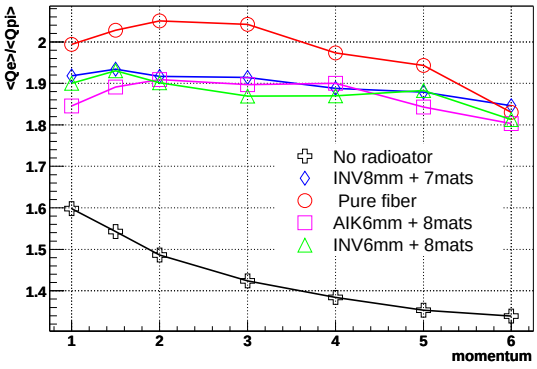

Figure 3.9: the ratio of most probable value of electron energy deposit to that of pion energy deposit as a function of beam momentum. The results are shown in case of radiator INV6, INV8, AIK6 and PP and in case of no radiator.

The ratios of mean pulse heights of electrons to those of pions as a function of drift region in case of beam momentum of 3 GeV/c (left) and 6 GeV/c (right) are shown in Fig. 3.10. The relationship between the drift region and the drift time is summarized in Table 3.3.

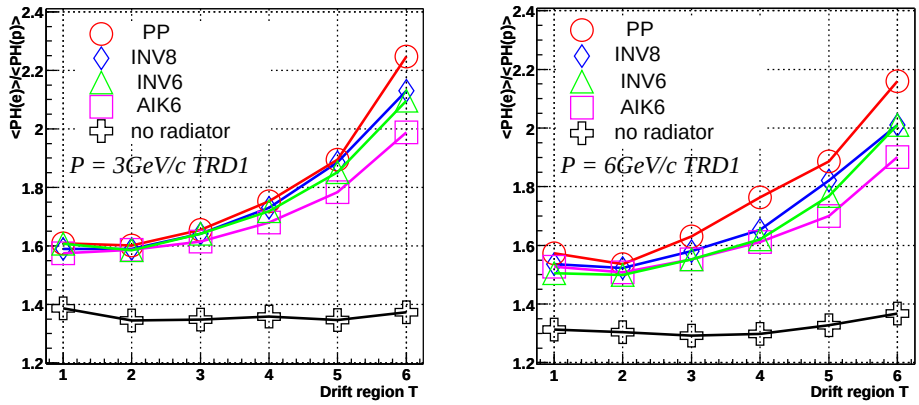

Figure 3.10: Mean relative electron/pion pulse heights as a function of drift region for all radiators. Left and right panel is in case of beam momentum of 3 GeV/c and 6 GeV/c, respectively.

Table 3.3: The definition of drift region.

Drift region	Drift time [μs]
1	0.35 - 0.70
2	0.70 - 1.05
3	1.05 - 1.40
4	1.40 - 1.75
5	1.75 - 2.10
6	2.10 - 2.45

The ratios for sandwich type radiators are smaller than that for PP fibers because of the self-absorption in PMI sheets. The ratios for beam momentum of 6 GeV/c are smaller for all radiators than those for the momentum of 3 GeV/c. This is because energy loss of pions at 6 Gev/c is larger compared to that of pions at 3 GeV/c, while energy loss of electrons and absorption of TR photon are almost constant for these beam momenta.

As shown in Fig. 3.7, the largest pulse height is seen mostly around the end of drift time in case of electron events and radiator used. Fig. 3.11 shows the distributions of the largest pulse heights which were measured at different drift time, 1.7 μs for the upper left, 1.9 μs for the upper right, 2.2 μs for the lower left and 2.4 μs for the lower right, respectively. As the largest pulse height was measured mostly at later drift time, the secondary peak is enhanced compared to the first peak. This means that the secondary peak is derived from the absorption of transition radiation and the energy loss, while the first peak is derived from only energy loss. The smooth lines in the Fig. 3.11 are the fitting results. The fitting function is the convolution of energy loss and the absorption of transition radiation. Dashed blue line corresponds to the function which describes the absorption of TR and collisional energy loss, dotted black line corresponds to the function which describes only collisional energy loss and was extracted from the data taken without radiator and the solid green line is the convolution of these two functions. These fitting functions will be described in detail in next chapter.

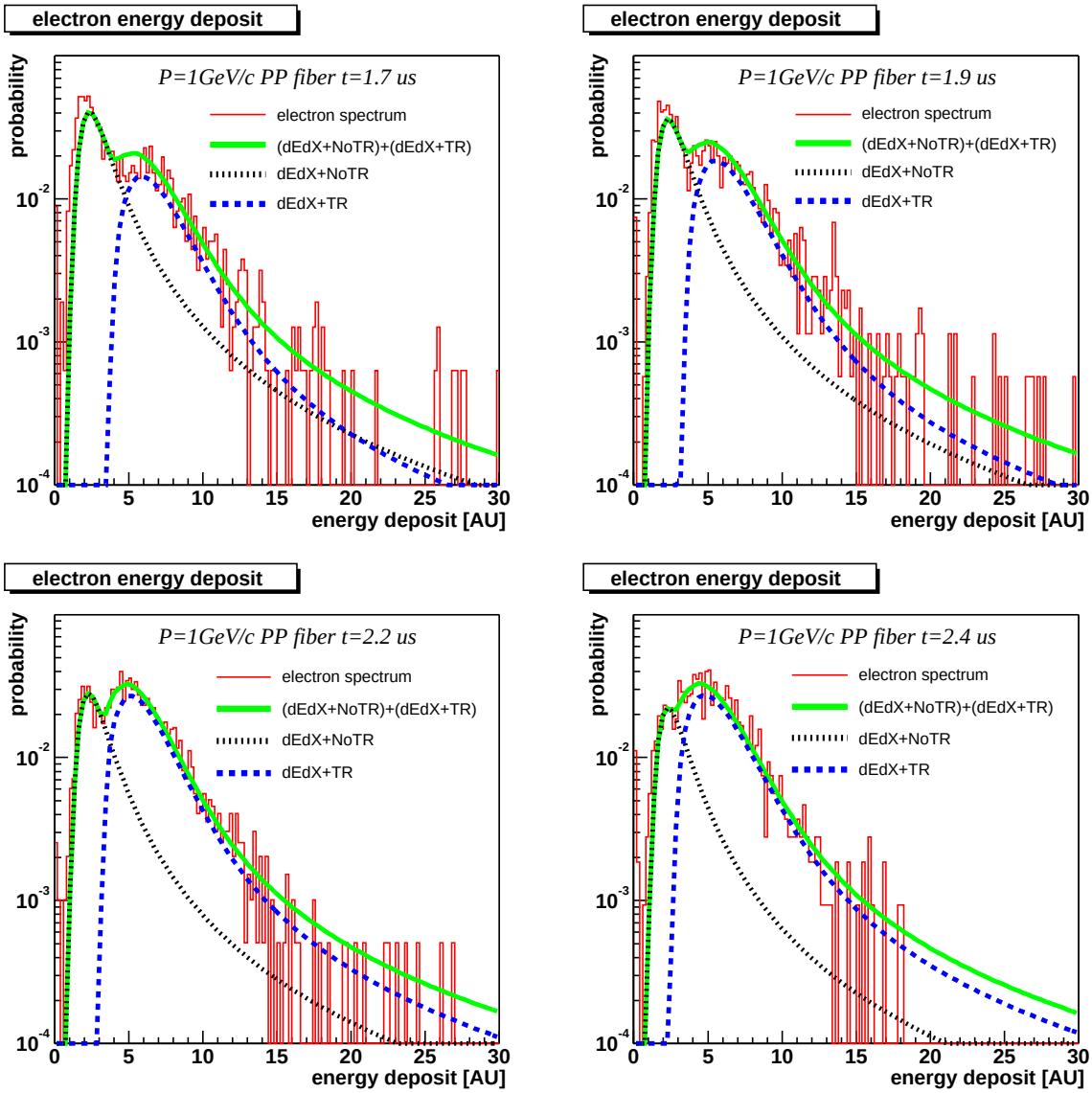

Figure 3.11: The distributions of energy deposit in different position.

Chapter 4

Analysis of the electron identification performance

In this chapter, the analysis procedure of electron identification performance of the prototype TRD and the results are described. The pion rejection factor is one of the useful information to describe the capability of electron identification.

4.1 Definition of pion rejection factor

The pion rejection factor is defined as the inverse of the pion misidentification probability, which is the ratio of number of pion events in the region defined by a certain electron efficiency (usually 90%) to the total pion events.

Electron efficiency, E_{eff}, is defined as follows:

$$E_{eff}(p) = \frac{N(e|p \leq P_e \leq 1)}{N(e|0 \leq P_e \leq 1)} \tag{4.1}$$

where P_e is the electron probability that a certain event is to be an electron and covers from 0 to 1, $N(e|p \leq P_e \leq 1)$ is the number of electron events whose electron probability is more than p and $N(e|0 \leq P_e \leq 1)$ is total number of electron events. In this analysis, electron probability is extracted by two methods: one is the Likelihood method and the other is neural network method.

Pion misidentification probability, $P_{\pi \to e}$, is defined as follow by using the electron probability where electron efficiency becomes 90%:

$$\mathrm{P}_{\pi \to \mathrm{e}} = \frac{N(\pi|p_{90\%} \leq P_e \leq 1)}{N(\pi|0 \leq P_e \leq 1)} \tag{4.2}$$

where $N(\pi|p_{90\%} \leq P_e \leq 1)$ is the number of pion events whose electron probability is more than $p_{90\%}$, $N(\pi|0 \leq P_e \leq 1)$ is the total number of pion events and $p_{90\%}$ satisfies the following relation:

$$0.9 = \frac{N(e|p_{90\%} \leq P_e \leq 1)}{N(e|0 \leq P_e \leq 1)} \tag{4.3}$$

Finally, the pion rejection factor is defined as follows:

$$\text{Pion rejection factor} = \frac{1}{P_{\pi \to e}} \tag{4.4}$$

4.2 Data sample and Event selection

In this section, data sample and event selection are described. It is necessary to classify electron events and pion events before electron identification capability is analyzed.

4.2.1 Event selection

The procedure of event selection for electron samples and pion samples is described below.

Separation of electrons and pions

Electrons and pions are separated with two air-filled Cherenkov counters and a Pb-glass calorimeter by setting thresholds. Figure 4.1 shows the correlation of responses between one Cherenkov detector and a lead-glass calorimeter for all momenta. Table 4.1 shows the thresholds of two Cherenkov counters and a lead-glass calorimeter for the classification of electrons and pions. These thresholds were decided to be able to define as many number of electron events and pion events as possible and to avoid each event class being misidentified as little as possible.

Table 4.1: Threshold values for event selection of electrons and pions

particle	momentum	Cherenkov1 [channel]	Cherenkov2 [channel]	lead-glass[channel]
electron	1 GeV/c	≥ 100	≥ 110	≥ 175
	1.5 GeV/c	≥ 50	≥ 60	≥ 270
	2 GeV/c	≥ 40	≥ 60	≥ 370
	3 GeV/c	≥ 60	≥ 60	≥ 600
	4 GeV/c	≥ 70	≥ 60	≥ 820
	5 GeV/c	≥ 65	≥ 60	≥ 1020
	6 GeV/c	≥ 120	≥ 120	≥ 1200
pion	1 GeV/c	≤ 6	≤ 10	≤ 85
	1.5 GeV/c	≤ 2	≤ 3	≤ 85
	2 GeV/c	≤ 2	≤ 3	≤ 86
	3 GeV/c	≤ 2	≤ 3	≤ 90
	4 GeV/c	≤ 6	≤ 9	≤ 90
	5 GeV/c	≤ 8	≤ 10	≤ 120
	6 GeV/c	≤ 20	≤ 20	≤ 120

Figure 4.2 shows the distributions of each Cherenkov counter and a lead-glass calorimeter after threshold cuts being applied by the other two detectors.

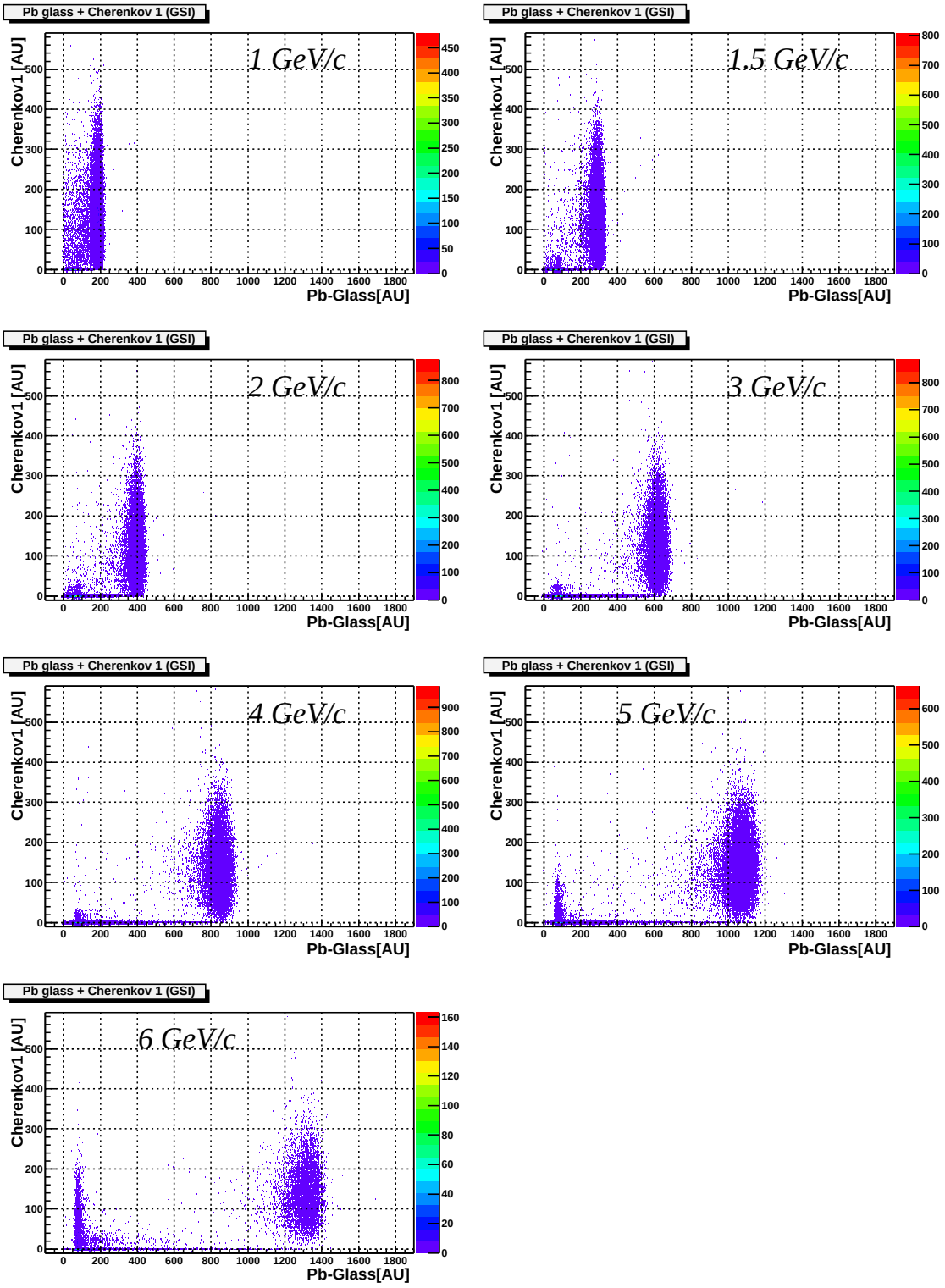

Figure 4.1: Correlation of the response between one Cherenkov detector and a lead-glass calorimeter for all momenta.

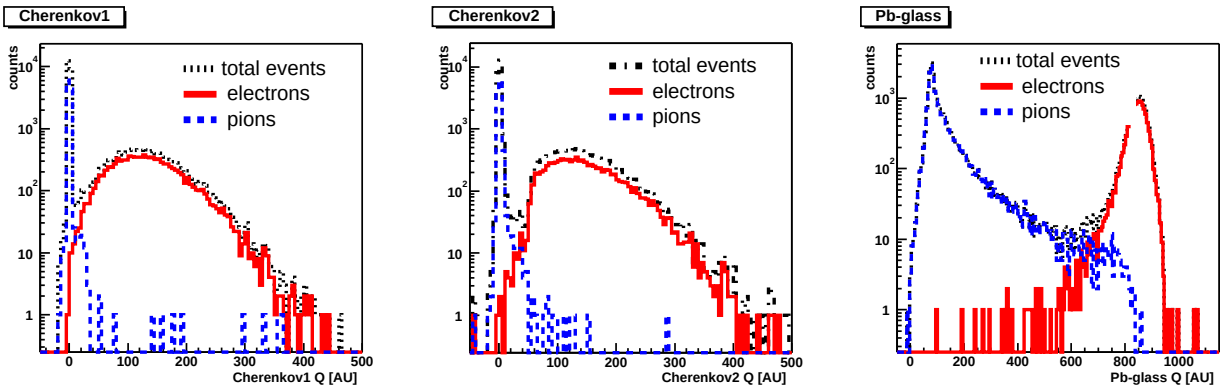

Figure 4.2: The distribution of each detector after cuts were applied. Beam momentum was 4 GeV/c. Left panel shows the distribution of Cherenkov1 after cuts were done by Cherenkov2 and a lead-glass calorimeter. Central panel shows the distribution of Cherenkov2 after Cherenkov 1 and a lead-glass calorimeter cuts were applied. The right panel shows the lead-glass distribution after two Cherenkov cuts were applied. Red (blue) line is the electron (pion) candidates after cuts being applied by the other two detectors.

Selection of good events with TRD

The number of readout pads of each TRD module was limited to be 8 during the test experiment. Figure 4.3 shows the distribution of hit position summed up for each drift time. Hit position was defined to be the pad number where maximum pulse height was measured.

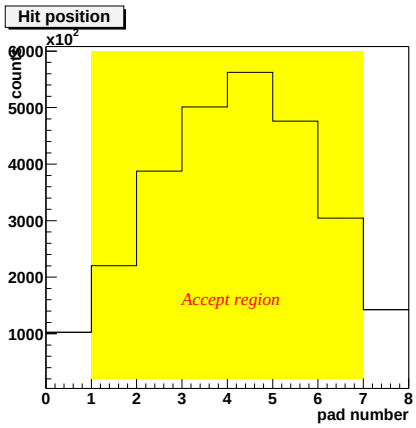

Figure 4.3: The distribution of hit position summed up for each 50 μs. The hit position was defined to be the pad number where maximum pulse height was measured. Yellow region is accept region which indicates that the events whose hit position belongs to the pad number from "1" to "6" are used in this analysis.

Since there exists the charge sharing effects between neighboring pads, the events whose hit position was pad number "0" or "7" were rejected.

4.3 Run Summary

In this section, run information which was used in this analysis is summarized. Radiator, beam momentum (P), incident angle with respect to readout plane (θ), magnetic field (B), number of total events (N_{total}), number of electron events (N_e) and number of pion events (N_π) are summarized in Table 4.2, Table 4.3 and Table 4.4. Table 4.2, Table 4.3 and Table 4.4 are the run information which was used to analyze radiator dependence, incident angle dependence and magnetic field dependence of electron identification capability, respectively.

4.4 Contaminations of data sample

The sample contamination was estimated by counting contaminations of pion events in the region of electron events and electron events in the region of pion events by applying the lead-glass cuts after discriminated by two Cherenkov counters. Table 4.5 is the result of the contamination. Contamination is negligible for the momenta below 5 GeV/c. At the beam momentum of 6 GeV/c, contamination is worse because pions can emit Cherenkov lights above 4.5 GeV/c.

Table 4.2: Summary of run information to be used to study radiator dependence of electron identification capability.

Radiator	P [GeV/c]	θ [degree]	B[T]	N_{total}	N_e	N_π
No radiator	1.0	15	0	43138	17617	3523
	1.5	15	0	42519	13270	7460
	2.0	15	0	61764	19335	14316
	3.0	15	0	42003	11741	9326
	4.0	15	0	41569	12038	8594
	5.0	15	0	41590	11591	5968
	6.0	15	0	17283	5393	1805
INV6	1.0	15	0	56480	17840	11312
	1.5	15	0	58413	13658	12035
	2.0	15	0	70914	15426	16758
	3.0	15	0	70300	15446	16275
	4.0	15	0	59165	14476	14099
	5.0	15	0	54775	14412	12401
	6.0	15	0	69391	19531	11385
INV8	1.0	15	0	47435	15192	9138
	1.5	15	0	44957	14896	13541
	2.0	15	0	62838	16694	17993
	3.0	15	0	57160	15537	16365
	4.0	15	0	57552	15693	16035
	5.0	15	0	37652	10357	8978
	6.0	15	0	37145	11508	8558
AIK6	1.0	15	0	37174	13854	6983
	1.5	15	0	43799	13549	12755
	2.0	15	0	42058	11980	12748
	3.0	15	0	42688	11623	14210
	4.0	15	0	41804	11851	13192
	5.0	15	0	42283	10666	11583
	6.0	15	0	47830	11991	12791
Pure fiber	1.0	15	0	51285	16715	12527
	1.5	15	0	52145	16149	17230
	2.0	15	0	51817	15529	18249
	3.0	15	0	52365	15755	18381
	4.0	15	0	63172	18707	19576
	5.0	15	0	55442	16568	16532
	6.0	15	0	18179	7076	4674

Table 4.3: Summary of run information to be used to study incident angle dependence of electron identification capability. In case of incident angle of 0 degree, the calorimeter wasn't in good operation and the calorimeter wasn't used to separate between electron events and pion events.

Radiator	P [GeV/c]	θ [degree]	B[T]	N_{total}	N_e	N_π
INV6	3.0	15	0	7685	2686	2658
	3.0	10	0	7153	2692	2627
	3.0	5	0	7071	2594	2689
	3.0	0	0	12738	4609	5945

Table 4.4: Summary of run information to be used to magnetic field dependence of electron identification capability. Since the trigger reduction wasn't applied, there were small number of electron events.

Radiator	P [GeV/c]	θ [degree]	B[T]	N_{total}	N_e	N_π
INV6	6.0	0	0	43342	745	17672
	6.0	0	0.14	54019	813	23042
	6.0	0	0.28	55497	790	23718
	6.0	0	0.42	52660	732	22523
	6.0	0	0.56	50027	600	20326

Table 4.5: contamination for all momenta.

momentum	contamination of pion events	contamination of electron events
1 GeV/c	0.6%	0.1%
1.5 GeV/c	0.10%	0.05%
2 GeV/c	0.08%	0.05%
3 GeV/c	0.09%	0.06%
4 GeV/c	0.20%	0.10%
5 GeV/c	0.43%	0.17%
6 GeV/c	1.73%	0.36%

4.5 Analysis Method-Likelihood ratio method

To analyze the classification capability with the prototype TRDs, likelihood ratio method was applied. Likelihood ratio method has been applied in the analysis of particle identification for various TRDs [12, 13, 14, 15, 16, 17, 18, 24].

The analysis procedure of likelihood ratio method is described in this section.

4.5.1 Definition of Likelihood ratio

The Likelihood ratio to be an electron is defined in Eq. 4.5 or equivalently Eq. 4.6.

$$L_e^1 = \log \frac{P_e}{P_\pi} \tag{4.5}$$

$$L_e^2 = \frac{P_e}{P_e + P_\pi} \tag{4.6}$$

Here electron probability, P_e, and pion probability, P_π, represent the probability that the event may be an electron or a pion, respectively. Likelihood ratio is evaluated for each track by using the ratio of electron probability to the pion probability. The decision of P_e and P_π depends on the observables which are used to classify the events into electrons or pions. In this analysis, following three approaches were applied.

1. LQ method : probabilities were obtained from total deposit energy in the TRD
2. LQX method : probabilities were obtained from total deposit energy in the TRD and the drift time when the largest pulse height was measured.
3. 2DLQ method : drift region was split into 6 regions. Probabilities were obtained from the deposit energy in each drift region.

4.5.2 Radiator dependence of pion rejection

The electron identification capability was analyzed for various radiators as listed in Table 3.1 by using three Likelihood ratio methods. Three Likelihood methods are explained in detail and the analysis results are shown.

LQ method

In the LQ method, the electron probability P_e and pion probability P_π were defined in the following relations, respectively:

$$P_e = \prod_{n=1}^{4} P(Q_n|e) \tag{4.7}$$

$$P_\pi = \prod_{n=1}^{4} P(Q_n|\pi) \tag{4.8}$$

When a track deposits total energy of Q_n in the n-th TRD, $P(Q_n|e)$ $[P(Q_n|\pi)]$ means probability for an electron [pion] to deposit its energy Q_n in the n-th TRD. To evaluate P_e and P_π, the total deposit energy distributions of four TRDs were extracted for electron events and pion events and normalized as shown in Fig. 3.6. To define the electron probability, P_e, and pion probability, P_π, the probability distribution functions have to be evaluated by fitting normalized distributions of total energy deposit in each TRD. Since the absorption of transition radiation photon and collisional energy loss contribute to the distribution of energy deposit in case of electrons, the probability distribution function is expected to be the convolution of the distribution of ionization and that of absorption of transition radiation photon. Let $f^e(Q)$ and $g^e(Q)$ be the electron normalized distribution function of energy loss by ionization and absorption of TR photons, respectively. Then the observed distribution for electrons is expected to be written:

$$h^e(Q) = \alpha f^e(Q) + (1-\alpha)\int f^e(Q-q)g^e(q)dq, \tag{4.9}$$

where α is the probability that TR photon isn't generated or isn't absorbed in the TRD. For the TR distribution term, $g^e(Q)$, the following function was chosen [24].

$$g^e(Q) = a(Q-Q_0)^b \exp[-c(Q-Q_0)] \tag{4.10}$$

where b was fixed to 1. The distribution function of energy loss is assumed to be Landau distribution and was decided from the measurement without radiator. The pion normalized distribution function was fitted with the convolution of Landau and Gauss distribution. The fitting results are shown in Fig. 4.4. Left panel is the probability distribution for pions with convolution of Landau and Gaussian fit and Right panel is that for electrons with Eq. 4.9 fit. The distribution of $\alpha f^e(Q)$ and $(1-\alpha)\int f^e(Q-q)g^e(q)dq$ are also shown for comparison. From these distribution functions, the electron probability and pion probability were obtained.

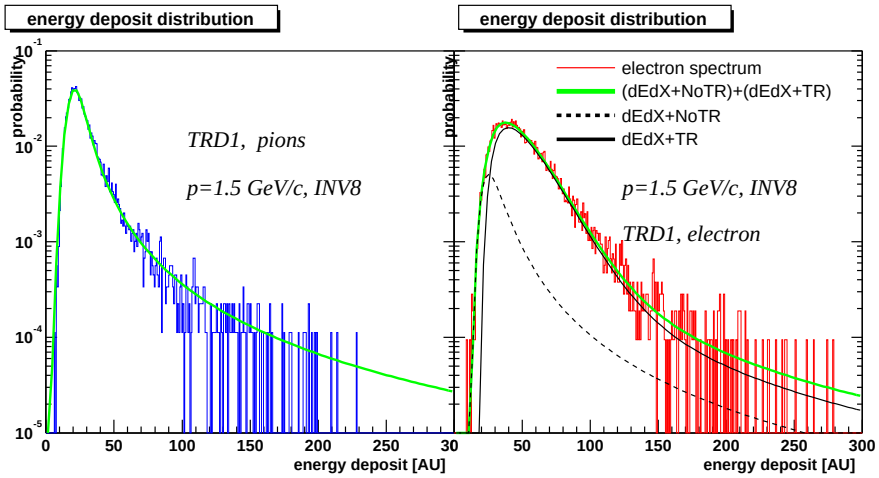

Figure 4.4: Pion probability distribution with pion spectrum (Left) and the electron probability distribution with electron spectrum (Right). Green line is the fitting results. In right panel, solid black line corresponds to the convolution of energy loss and absorption of TR, while dashed black line corresponds to only energy loss.

Figure 4.5 shows the distributions of the Likelihood ratio to be an electron for one to four TRD layers in case of INV8 radiator and beam momentum of 1.5 GeV/c. Solid line and dashed line are Likelihood distribution for electrons and pions, respectively. The arrow indicates the region of electron efficiency of 90%.

The pion misidentification probability is defined as a fraction of pion yields in the region where electron efficiency is more than 90% to the total pion yields. The pion misidentification probabilities at 90% electron efficiency were obtained to be 34.4%, 16.6%, 7.8% and 3.9% for 1, 2, 3 and 4 TRD layers, respectively. As the number of TRD layers increases, better separation

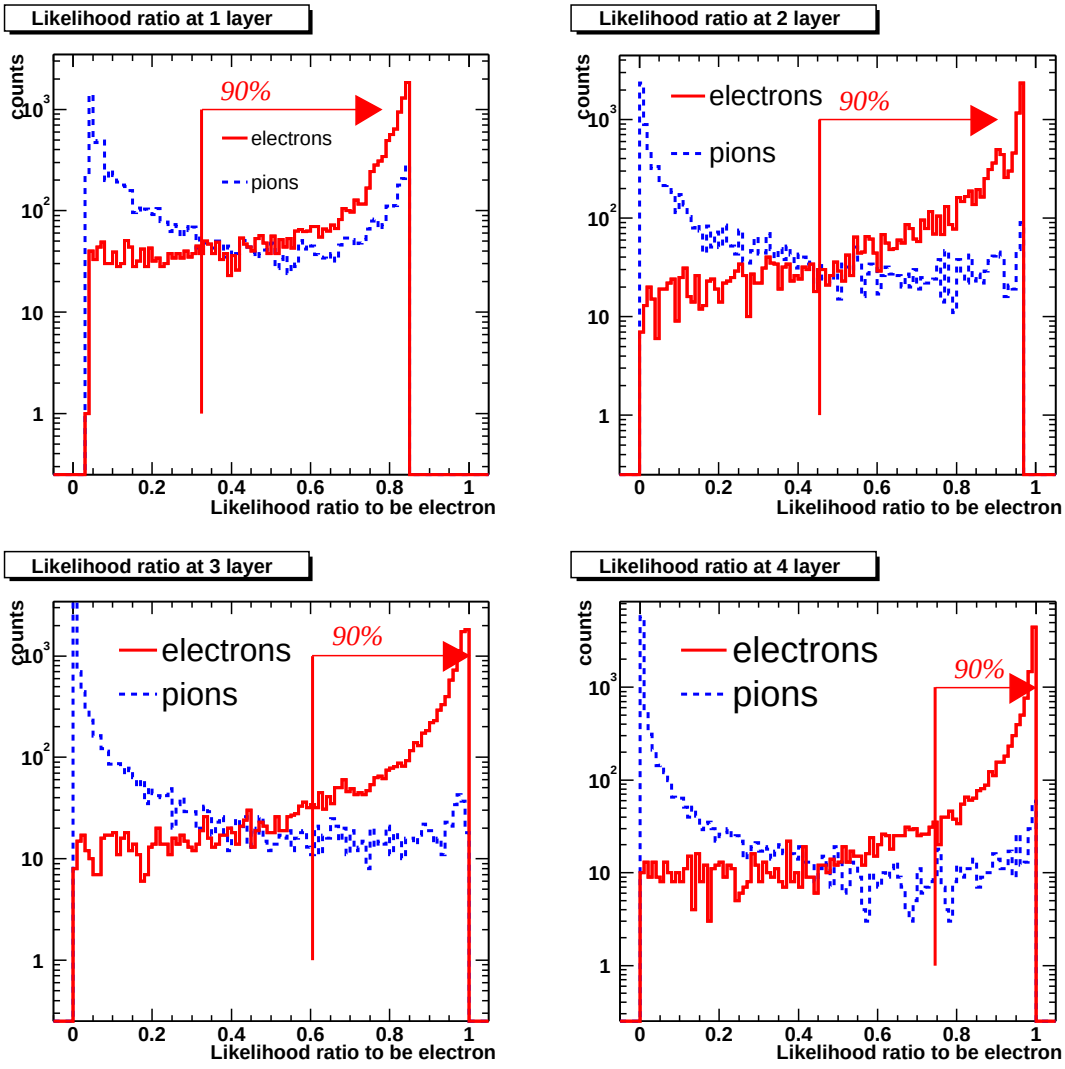

Figure 4.5: Likelihood distribution for electrons and pions in case of 1, 2, 3, 4 TRD layers. The arrow indicates the region where the electron detection efficiency is 90%. Radiator is INV8 and beam momentum is 1.54 GeV/c.

is achieved. The pion misidentification probability by using 6 TRD layers was extrapolated from the dependence of number of TRD layers as shown in Fig. 4.6. Pion misidentification

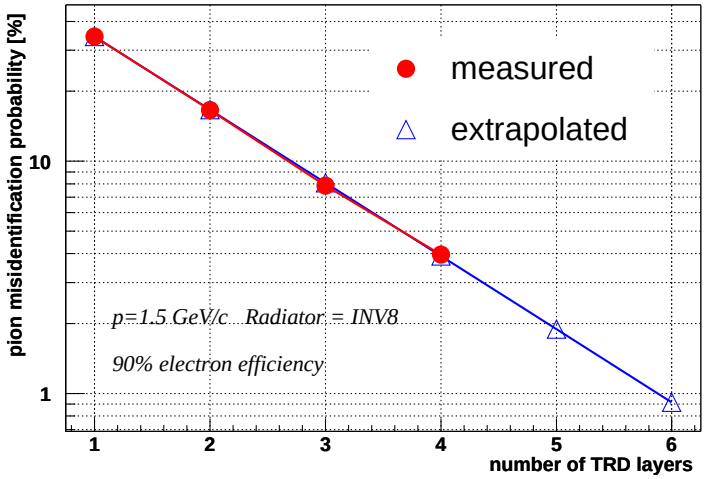

Figure 4.6: Pion misidentification probability as a function of number of TRD layers. Circle means the measured value and triangle means the extrapolated value.

probability of 0.88%, which corresponds to pion rejection factor of 113, was achieved at 6 TRD layers. The pion rejection factor for INV6, INV8, AIK6, PP radiators as a function of momentum is shown in Fig. 4.7. The result in case of no radiator is also shown for comparison. The PP radiator achieves the best pion rejection and almost the same tendency can be seen for INV6, AIK6 and INV8 radiator. When the momentum is larger than 3 GeV/c, the pion rejection becomes worse and is less than 100. This is due to larger pion energy loss, while the electron energy loss is constant.

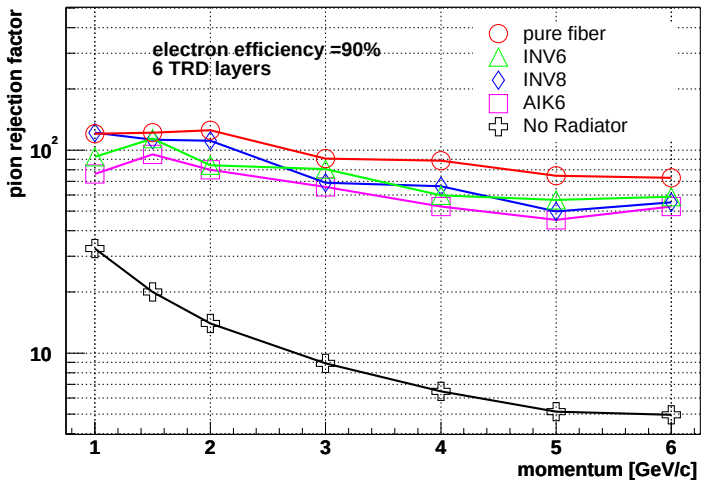

Figure 4.7: pion rejection factor as a function of momentum extrapolated to 6 TRD layers at electron efficiency of 90%.

LQX method

Since the TR contribution can be seen around the end of drift time, the information on the arrival time of largest cluster created in the drift region could be used to improve the pion rejection. In this analysis, the electron probability P_e and pion probability P_π are defined in the following relations,

$$P_e = \prod_{n=1}^{4} P(Q_n|e) \times P(T_n|e) \tag{4.11}$$

$$P_\pi = \prod_{n=1}^{4} P(Q_n|\pi) \times P(T_n|\pi) \tag{4.12}$$

where the definition of $P(Q_n|e)$ and $P(Q_n|\pi)$ are the same as those in the LQ method and $P(T_n|e)$ $[P(T_n|\pi)]$ represents the probability that the largest pulse height derived from electron [pion] is measured at the drift time of T_n in the n-th TRD. The probability distribution of the arrival time of the largest cluster is shown in Fig. 4.8. Solid line is for electrons and dashed line is for pions. It is seen that the largest cluster is measured at the end of drift time in case of electrons.

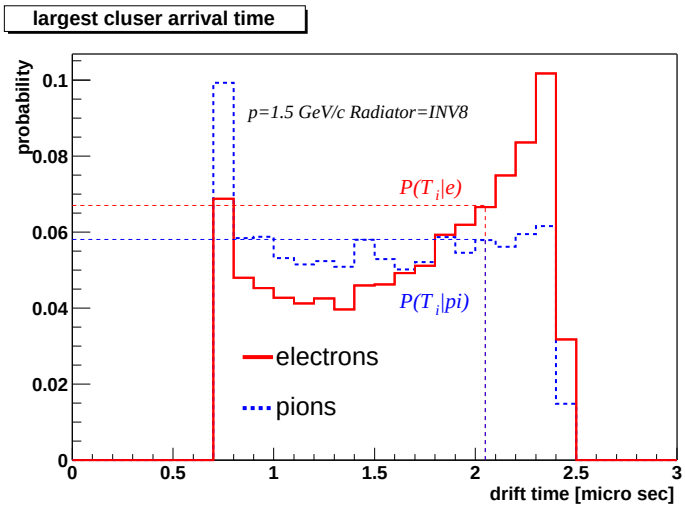

Figure 4.8: The probability distribution of the arrival time of largest cluster generated in the drift region of TRD1. Solid line is that for electrons and dashed line is that for pions.

Figure 4.9 shows the likelihood ratio distributions based on LQX method. Pion misidentification probabilities at 90% electron efficiency were obtained to be 33.5%, 15.4%, 6.5% and 3.4% for 1, 2, 3 and 4 TRD layers, respectively. From the result of the extrapolation to 6 TRD layers as shown in Fig. 4.10, the pion misidentification probability of 0.67% was achieved, which corresponds to the pion rejection factor of 150. Better pion rejection factor was achieved in the LQX method. The pion rejection factor for all radiators as a function of momentum based on LQX method is shown in Fig. 4.11. The pion rejection is improved and within requirement for all momenta in case of PP fibers and for below 3 GeV/c in case of other radiators.

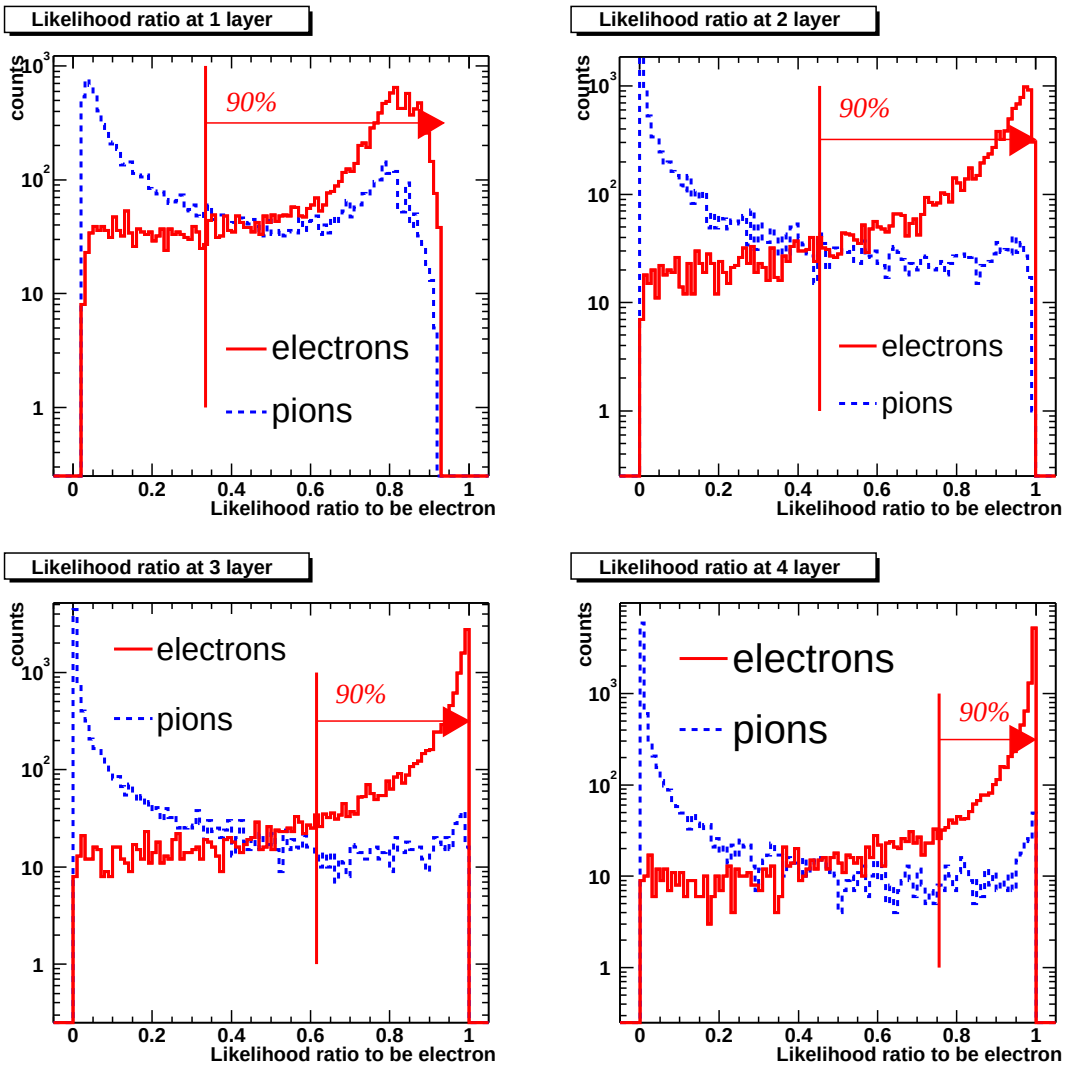

Figure 4.9: Likelihood distribution for electrons and pions in case of 1, 2, 3, 4 TRD layers. The arrow indicates the region where the electron detection efficiency is 90%. Radiator is INV8 and beam momentum is 1.5 GeV/c.

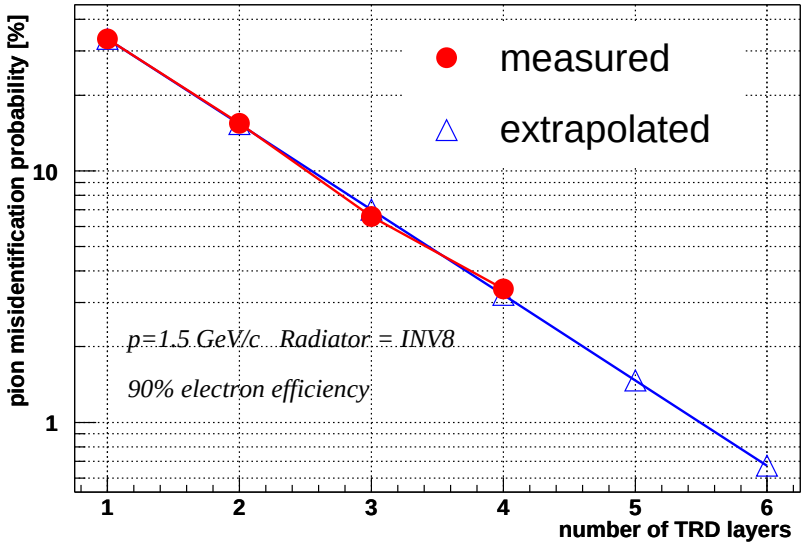

Figure 4.10: Pion misidentification probability as a function of number of TRD layers. Circle means the measured value and triangle means the extrapolated value.

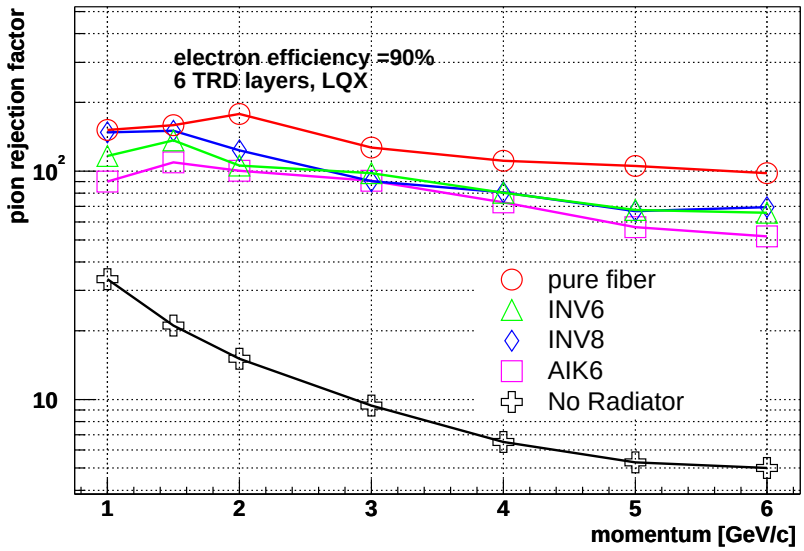

Figure 4.11: Pion rejection factor based on LQX method as a function of beam momentum. The pion rejection factor is extrapolated to 6 TRD layers at electron efficiency of 90%.

2DLQ method

Since the pulse height of electron events has a strong position dependence and has a large spike around the end of drift time, utilizing the correlation between the pulse height and the drift region could provide better performance of pion rejection. The drift region was divided into 6 regions as shown in Fig. 4.12. Number of regions was optimized by checking its dependence of pion rejection factor. In the 2DLQ analysis, the P_e and P_π are defined in the following relations,

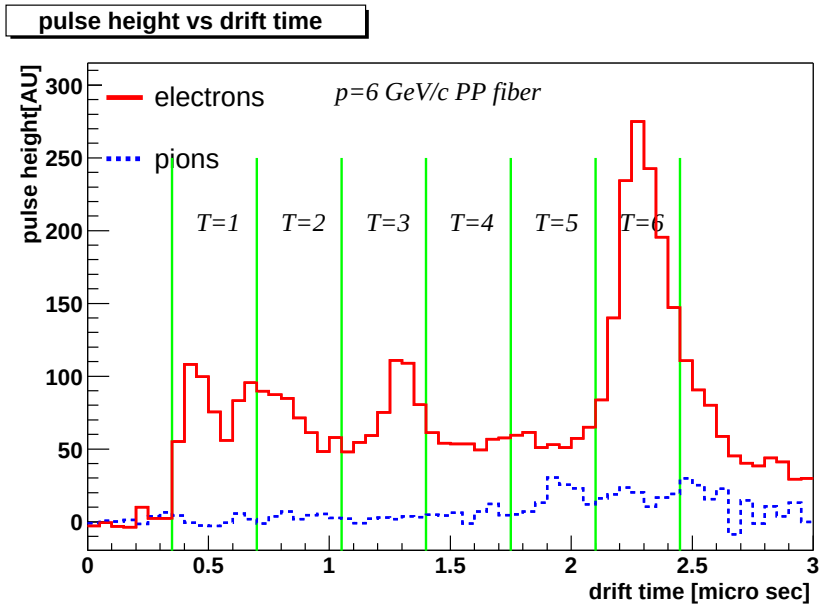

Figure 4.12: The divided drift region. The energy deposit in the drift region from T0 to T6 were used for 2DLQ analysis.

respectively.

$$P_e = \prod_{n=1}^{4} \prod_{T=1}^{6} P(Q_n^T|e) \tag{4.13}$$

$$P_\pi = \prod_{n=1}^{4} \prod_{T=1}^{6} P(Q_n^T|\pi) \tag{4.14}$$

Here, T denotes the section number of the drift region, which covers from 1 to 6. To define the $P(Q_n^T|e)$ and $P(Q_n^T|\pi)$, the deposit energy distributions for electrons and pions in each section of the TRD were extracted. For example, the distributions of energy deposit for electrons and pions in first, third and sixth region are shown in Fig. 4.13 including the fitting results. Fitting function is the same as Eq. 4.9. From the distribution functions, the electron probability and pion probability were defined for each section. The likelihood ratio distributions for 1, 2, 3, 4 TRD layers were extracted as shown in Fig. 4.14. The pion misidentification probabilities at electron efficiency of 90% are 32.0%, 13.0%, 4.7% and 2.3% for 1, 2, 3, and 4 TRD layers, respectively. From the result of the extrapolation to 6 TRD layers as shown in Fig. 4.15, the pion misidentification probability of 0.38% was achieved, which corresponds to the pion rejection factor of 263. The pion rejection factor was improved by the 2DLQ method.

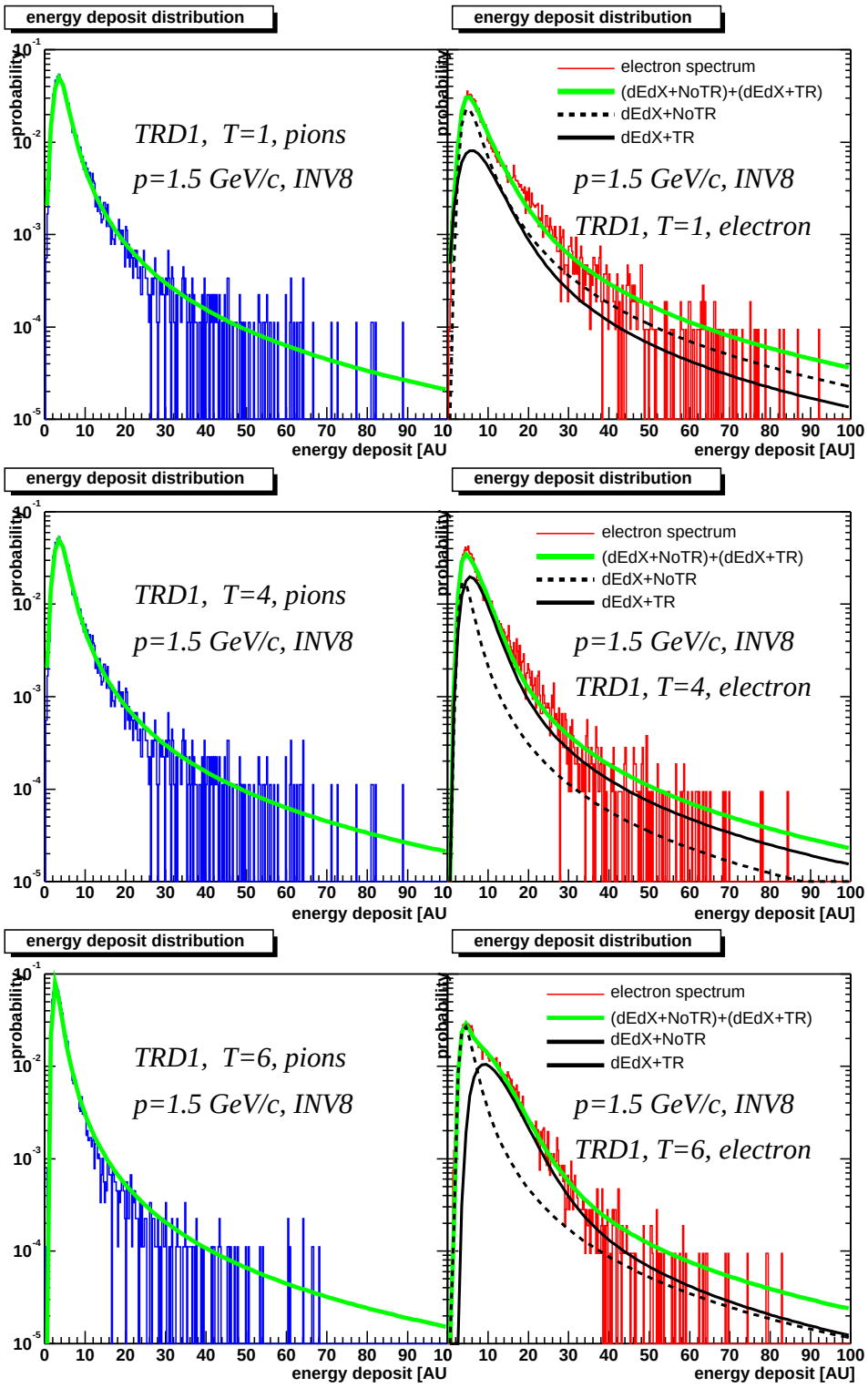

Figure 4.13: The deposit energy distribution's for electrons and pions in the sixth drift region at 1.5 GeV/c. Smooth lines are fitting results,, where fitting function is defined in eq. 4.9.

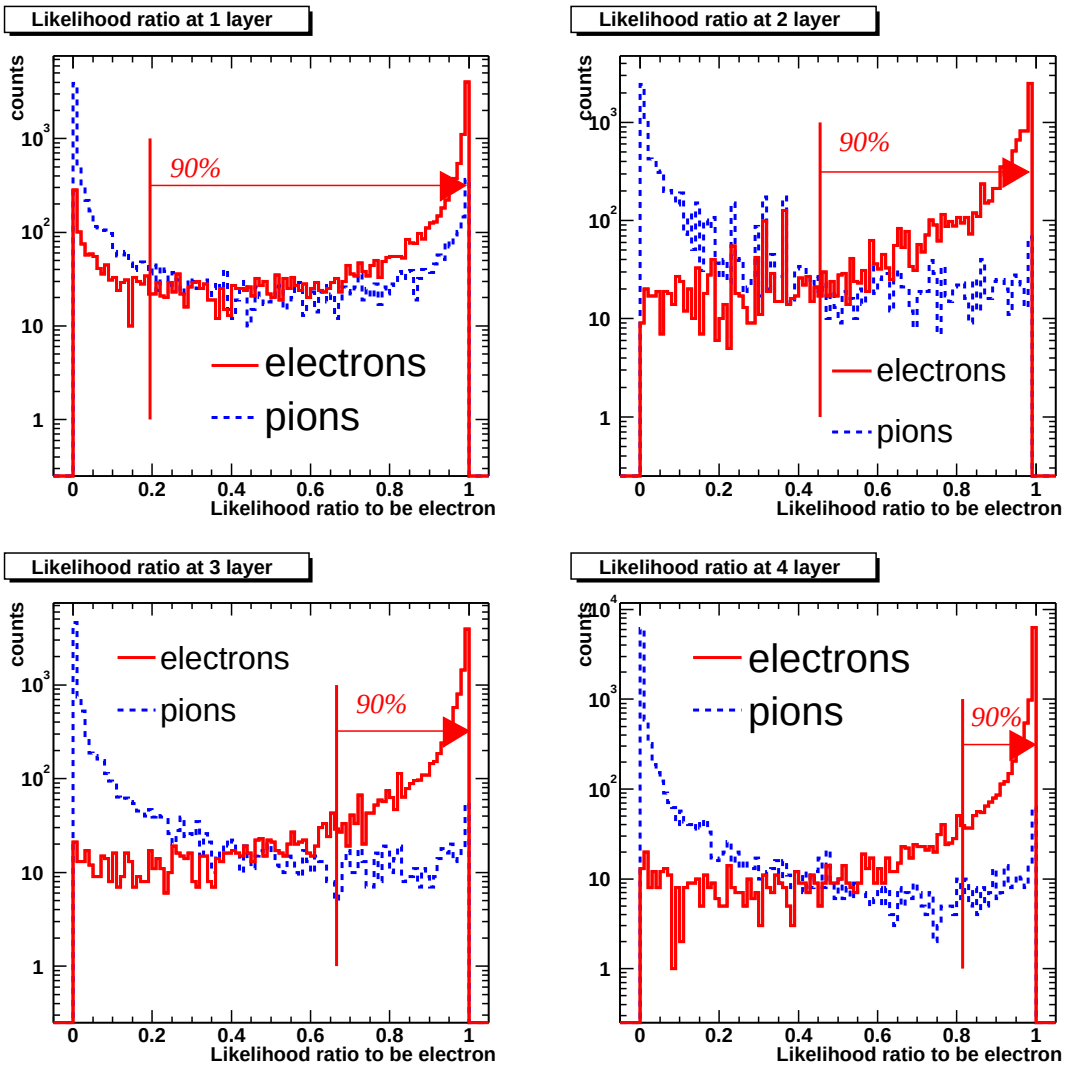

Figure 4.14: Likelihood distribution for electrons and pions in case of 1, 2, 3, 4 TRD layers based on 2DLQ method. The arrow indicates the region where the electron detection efficiency is 90%. Radiator is INV8 and beam momentum is 1.5 GeV/c.

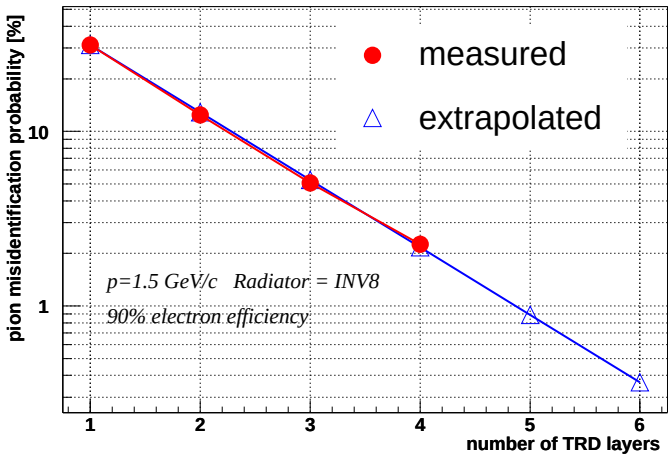

Figure 4.15: Pion misidentification probability as a function of number of TRD layers. Circle means the measured value and triangle means the extrapolated value.

The pion rejection factor for all radiators as a function of momentum is shown in Fig. 4.16. The pion rejection factor was greatly improved compared with the results based on previous analysis methods as shown in Table 4.6. From Fig. 4.16, pion rejection factor of above 100 is achieved for all radiators except beam momentum of 6 GeV/c.

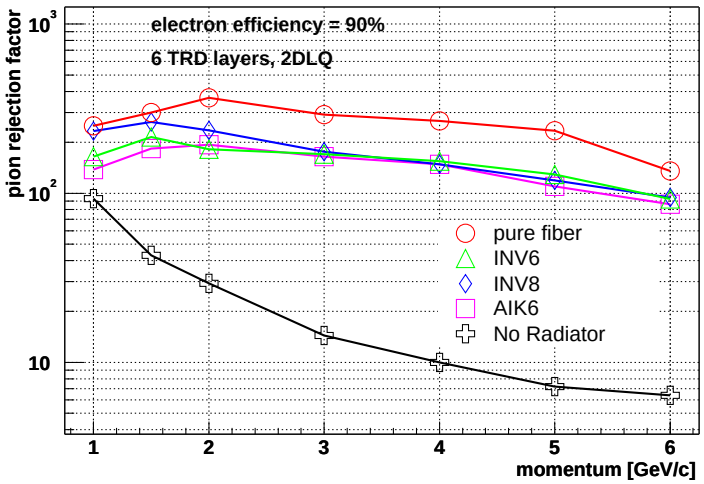

Figure 4.16: Pion rejection factor based on 2DLQ method as a function of beam momentum. The pion rejection factor is extrapolated to 6 TRD layers at electron efficiency of 90%.

Table 4.6: Comparison of the results of pion rejection factor at 6 TRD layers based on LQ method, LQX method and 2DLQ method.

Radiator	Method	1 GeV/c	1.5	2	3	4	5	6
INV6	LQ	92.6	113.6	84.0	80.6	89.9	56.8	58.8
	LQX	116.6	136.4	105.6	98.0	80.3	67.6	65.8
	2DLQ	164.7	214.7	181.7	170.5	154.5	129.4	92.6
INV8	LQ	122.0	112.4	111.1	69.0	66.2	49.8	55.3
	LQX	148.1	150.4	123.3	90.3	80.6	66.7	69.4
	2DLQ	233.4	263.8	235.5	176.3	147.9	119.3	94.2
AIK6	LQ	76.3	95.2	80.0	65.8	52.6	45.2	52.6
	LQX	90.0	109.3	100.5	90.9	73.0	56.8	51.8
	2DLQ	137.8	183.8	193.8	164.2	147.9	109.6	85.9
Pure fibers	LQ	120.5	122.0	125.0	90.9	88.5	74.6	73.0
	LQX	151.5	158.7	177.9	127.1	111.1	105.3	98.0
	2DLQ	249.7	299.9	366.4	291.8	267.8	233.9	135.4
No radiator	LQ	32.7	20.0	14.0	8.90	6.48	5.14	4.96
	LQX	33.6	21.1	15.0	9.38	6.51	5.29	5.00
	2DLQ	92.9	43.0	29.3	14.4	10.0	7.2	6.39

4.6 Analysis Method-Neural Network method

To analyze the classification capability with the prototype TRDs, neural network method was also applied. Neural network has been well-known as the pattern recognition method in the biological fields and astronomy [25] and has been begun to be applied in the fields of high energy physics [26, 27, 28, 29, 30]. There are few examples that the neural network was applied in the study of particle identification with TRD. Therefore the neural network can be a new analysis method in the study of particle identification with the TRD.

Since the signal patterns of electron events are greatly different from those of pions. The existence of the enhancement of the pulse heights around the end of the drift time is the key to distinguish a certain track to be an electron one. Therefore the neural network can be applied in this analysis as the pattern recognition method. Neural network may improve pion rejection because neural network can find the difference in the signal patterns of electrons and pions, especially the existence of enhancement of pulse heights around the end of drift time. In this neural network analysis, "multi-layered feed forward neural network" is used as a network structure as shown in Fig. 4.17. One of the features of the multi-layered feed-forward neural network is that the data flows only from the input layer to the output layer as shown in Fig. 4.17.

The 24 neurons were prepared in the input layer. To compare the pion rejection based on the 2DLQ analysis, the same 24 information, the deposit energy in each section of the TRD, was fed into these 24 neurons. According to Kolmogorov theorem [31], 49 neurons were prepared in the hidden layer. The task of hidden layer is to build up the internal representation of the input data. The 2 neurons were prepared in the output layer. One neuron is excited for electron

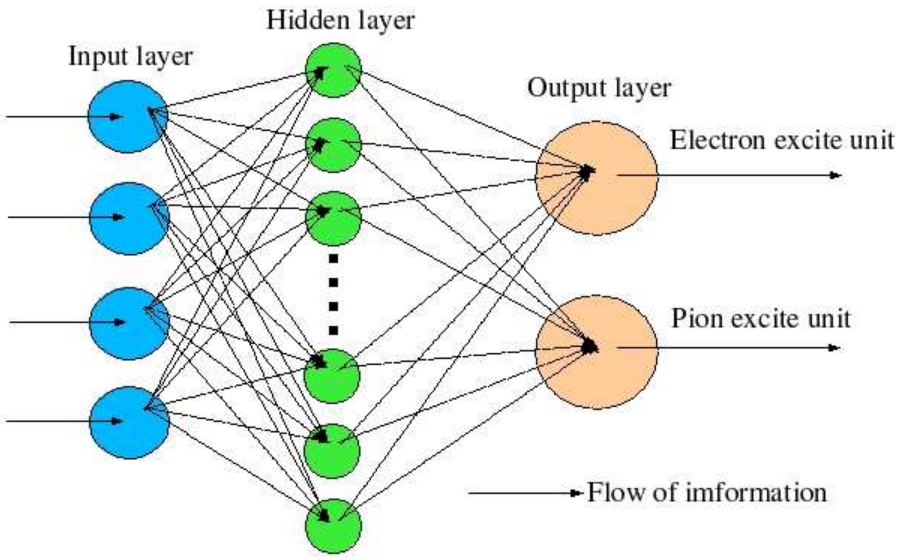

Figure 4.17: The structure of multi-layered feed forward network applied in the analyis.

events, called electron excite unit, and the other is excited for pion events, called pion excite unit. Each neuron in the input layer, denoted by i, connects to each neuron in the hidden layer, denoted by j, with the connection weight W^1_{ji}. In the same way, each neuron in the hidden layer connects to each neuron in the output layer, denoted by k, with the connection weight W^2_{kj}. The transfer function is described by the sigmoid function:

$$f(x,\theta) = \frac{1}{1+\exp(-g(x-\theta))}, \tag{4.15}$$

where g ($g > 0$) is the gain factor and θ is the threshold. The transfer function corresponds to the response of the neuron in the brain to the input information. If $x \geq \theta$, $f(x,\theta)$ is more than 0.5, which corresponds to the state that the neuron excites by receiving the signal x.

The output value of the neuron j in the hidden layer, denoted by H_j, is described in the following relation:

$$H_j = f(\sum_{i=1}^{24} W^1_{ji} X_i + \theta_j) \tag{4.16}$$

where the input information are represented to be X_i ($i = 1,\ 2,\ 3, \cdots,\ 24$), which are the deposit energy in each section of the TRD and θ_j is the threshold value.

The output values O_k from the output layer can be described in the following relation:

$$O_k = f(\sum_{j=1}^{49} W^2_{kj} H_j + \theta_k) \tag{4.17}$$

After the input information being transfered to the output layer, the probability that a certain event is to be an electron or a pion is obtained as the output value O_1 or O_2, respectively.

As the learning algorithm, the "back-propagation method" was applied in this analysis. The connection weights W^1_{ji} and W^2_{kj} are trained and updated after each pattern has been transfered

from the input layer to the output layer. The relation between the update weights and the previous weights are as follows:

$$W^s_{mn}|_{new} = W^s_{mn}|_{old} + \Delta W^s_{mn}|_{new} \tag{4.18}$$

Here $\Delta W^s_{mn}|_{new}$ is defined as follows:

$$\Delta W^s_{mn}|_{new} = -\eta \frac{\partial E_p}{\partial W^s_{mn}}\Big|_{W=W|_{old}} + \alpha \Delta W^s_{mn}|_{old} \tag{4.19}$$

Here $\Delta W^s_{mn}|_{old}$ refers to the previous updating and is introduced to avoid the connection weights from oscillating. η is the learning rate and α is the momentum factor and they satisfy $|\eta| \leq 1$ and $|\alpha| \leq 1$. E_p is the error function for a certain input pattern p, whose input pattern vector is $X^p = (X^p_1,\ X^p_2,\ X^p_3, \cdots,\ X^p_{24})$. The E_p is defined as follows:

$$E_p = \frac{1}{2}\sum_{k=1}^{2}(T_k - O^p_k)^2, \tag{4.20}$$

where O^p_k is the output value of the k-th neuron in the output layer for the input pattern p and T_1 and T_2 are the "teach signals", whose values are set as the expected values. In case of electron events, these signals are defined as follows:

$$\begin{cases} T_1 = 0.99 \text{ (excite state)} \\ T_2 = 0.01 \text{ (unexcite state)} \end{cases} \tag{4.21}$$

In case of pion events, T_1 and T_2 are defined as follows:

$$\begin{cases} T_1 = 0.01 \text{ (unexcite state)} \\ T_2 = 0.99 \text{ (excite state)} \end{cases} \tag{4.22}$$

The important point of this algorithm is that the connection weights are updated as the output values approach to the "teach signals" (ie. expected values), which is easy to demonstrate by using Eq. 4.18 and Eq. 4.19. The mean error for N events is defined by Eq. 4.23.

$$E = \frac{1}{N}\sum_p E_p \tag{4.23}$$

In this analysis, the network parameters, g, θ, η and α, are fixed after checking their dependences of pion rejection as follows:

$$\begin{aligned} g &= 1.0 \\ \theta &= 0.0 \\ \eta &= 0.002 \\ \alpha &= 0.005 \end{aligned} \tag{4.24}$$

Two data sets were prepared. One was used to fix the connection weights by teaching the data to the network. This set is called "learning data". The other data set is to test the generalization performance after the weights are fixed and used to evaluate the pion rejection. This set is

called "test data". The number of samples for learning data and test data is 8000 and 2000 for both electrons and pions below 4 GeV/c, respectively. For 5 GeV/c and 6 GeV/c, because of less statistics, 6000 and 2000 were prepared for learning data and test data, respectively.

Figure 4.18 shows the output distributions of the electron excite unit for learning data after 10 (left panel) and 1000 (right panels) learning cycles. "Learning cycle" means how many times the learning data is transfered to the network. The more events the network learns, the clearer the separation becomes. The efficiency, which is the fraction of number of events whose output

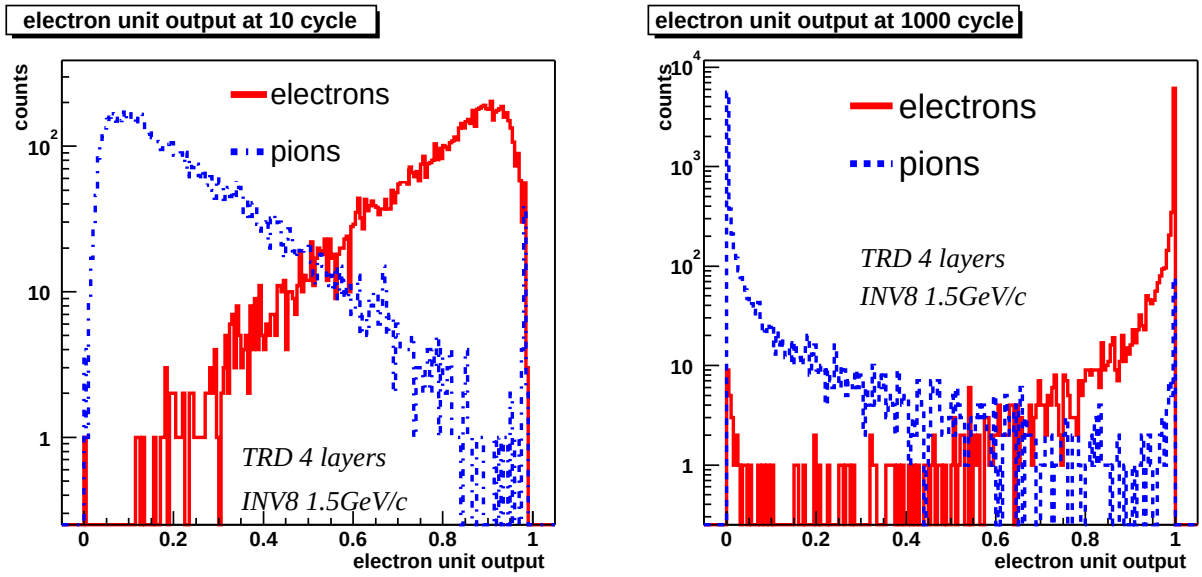

Figure 4.18: Electron excite unit output distributions when data sample were transfered 10 times (left panel) and 1000 times (right panel).

value of electron excite unit is over 0.5 for electrons and below 0.5 for pions, as a function of learning cycle is shown in Fig. 4.19. Solid red line, solid blue line, dashed red line and dashed blue line is for learning data of electrons, learning data for pions, test data for electrons and test data for pions, respectively. The efficiency grows up sharply up to 10 cycle and increases rather slowly after 10 cycles. After 100 cycles, the 97% of electron events excite the electron excite unit and 95% pions don't excite the electron excite unit. It is seen in the figure that the classification performance for the test data is worse compared with that for the learning data. This implies the occurrence of the generalization problem, that is the network cannot respond more correctly to the unknown data set even if the network can respond to the learning data more correctly. Figure 4.20 shows the mean error defined in Eq. 4.23 for learning data (solid) and test data (dashed) as a function of number of learning cycles. Error decreases sharply up to 10 cycles. This implies that network learns to respond as it is expected. For test data, the mean error becomes slightly worse due to the generalization problem.

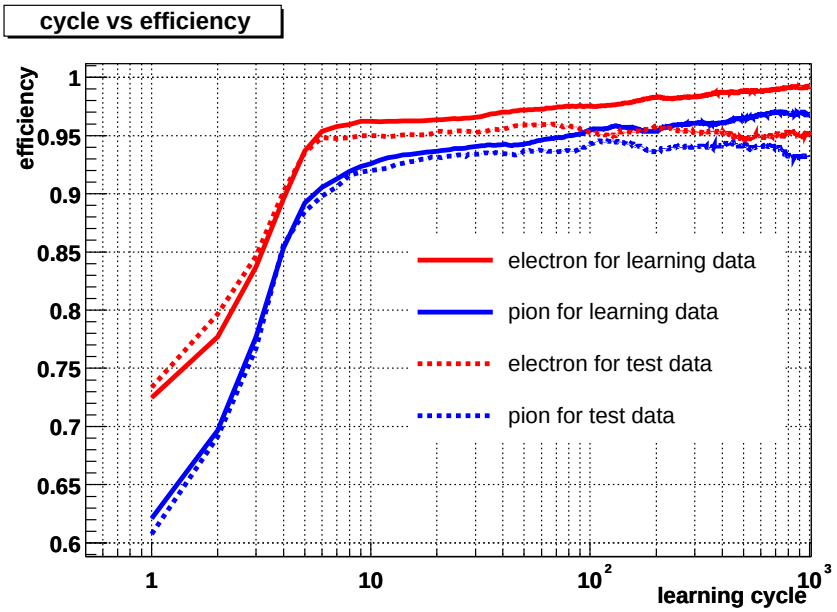

Figure 4.19: Efficiency as a function of learning cycle. Solid and dashed lines are efficiency for learning data and test data, respectively.

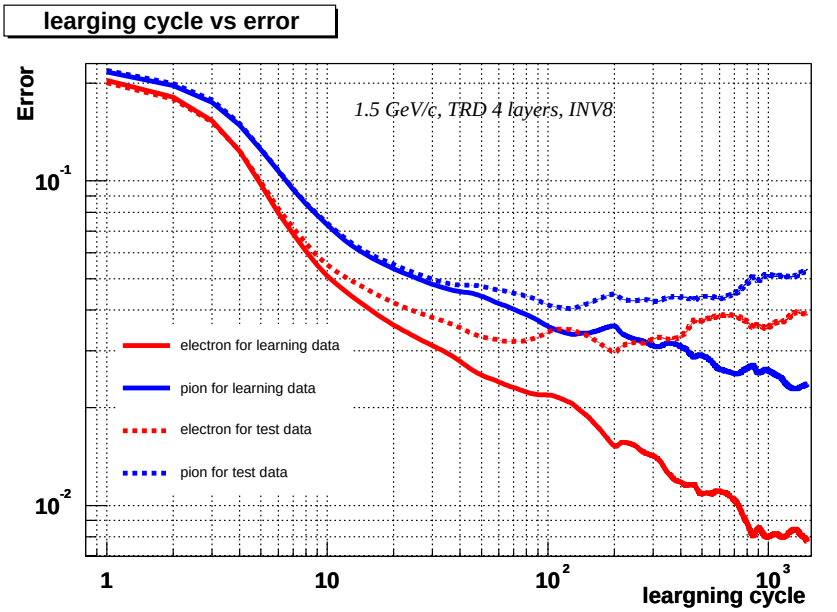

Figure 4.20: Mean error evolution for learning data (solid lines) and test data (dashed lines) as a function of number of learning cycle.

After the connection weights were fixed with 1500 learning cycles, the responses of the neural network for 1, 2, 3 and 4 TRD layers were extracted to check the capability of classification for the known data set. Figure 4.21 shows the distributions of the output of electron excite unit for the learning data. The pion misidentification probabilities at electron efficiency of 90% are 29.0%, 10.0%, 3.2% and 1.0% for 1, 2, 3, and 4 TRD layers, respectively. The comparison of pion misidentification probability for the learning data based on neural network method to that based on 2DLQ method is summarized in Table 4.7. From these results, it is demonstrated

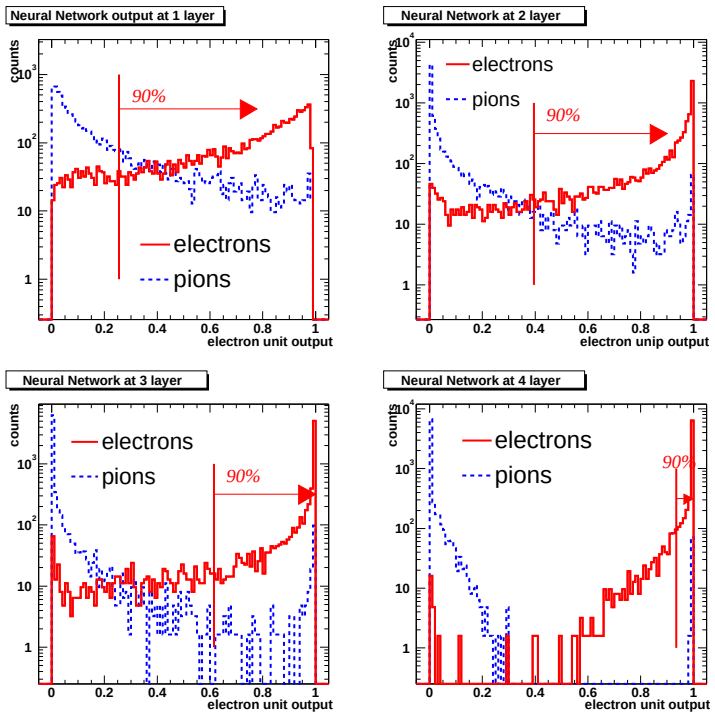

Figure 4.21: The output distributions of electron excite unit for learning data. Upper left figure is the distribution for 1 TRD layer. Upper right figure is the distribution for 2 TRD layers. Lower left figure is the distribution for 3 TRD layers. Lower right is that for 4 TRD layers. Radiator is INV8 and beam momentum is 1.5 GeV/c.

Table 4.7: Comparison of pion misidentification probability as a function of number of TRD layers extracted for learning data based on neural network method and 2DLQ method. Radiator is INV8 and beam momentum is 1.5 GeV/c.

method	1 layer	2 layers	3 layers	4layers
2DLQ	31.2%	12.4%	5.1%	2.3%
Neural network	29.0%	10.0%	3.2%	1.0%

that the neural network can be applied to the electron identification analysis and may improve pion rejection.

The correlation between the output value of electron excite unit and the input patterns, which demonstrates how the network identifies electrons, is shown in Fig. 4.22. The open circle represents for the value of electron excite unit above 0.8, which indicates the network identifies the event to be an electron. On the other hand, the open triangle means the value of electron excite unit output less than 0.5, which indicates the network identifies the event to be a pion. From Fig. 4.22, the network identifies the event to be an electron when the input patterns have enhancement of pulse heights around the end of drift time, while the network identifies the event to be a pion when there doesn't exist such an enhancement around the end of drift time. Therefore, the network distinguishes electrons from pions by judging the existence of the enhancement of pulse heights, which matches to the expectations. Figure 4.23

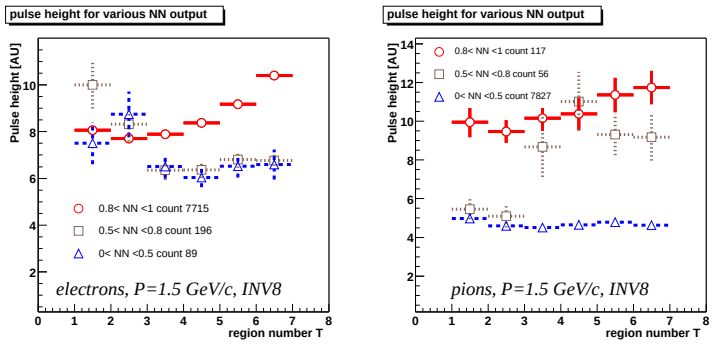

Figure 4.22: The input patterns of pulse heights for various electron excite unit output range. Left and Right panel are the input patterns for electrons and pions, respectively. Open circle, open square and open triangle correspond to the output range from 0.8 to 1.0, from 0.5 to 0.8 and from 0 to 0.5, respectively.

shows the correlation between the results based on neuron network and the results based on 2DLQ likelihood method. The neural network has the same tendency as 2DLQ method such that the output values of electron excite unit are almost unity for electron events and almost zero for pion events.

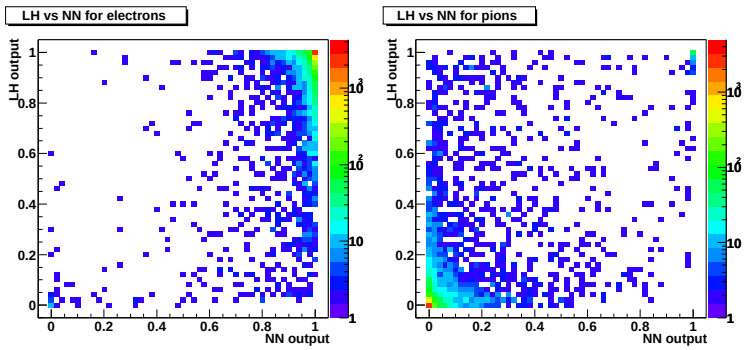

Figure 4.23: correlation between electron excite unit outputs and likelihood ratio for electron events (left panel) and pion events (right panel).

To evaluate the pion rejection factor, the test data set which hasn't been known to the network was fed into the input layer. The connection weights were fixed when the mean error for the test data of pions reached minimum. The distributions of the electron excite unit output for 1, 2, 3 and 4 TRD layers are shown in Fig. 4.24. The pion misidentification probabilities at electron efficiency of 90% are 31.0%, 11.8%, 4.6% and 2.1% for 1, 2, 3, and 4 TRD layers, respectively.

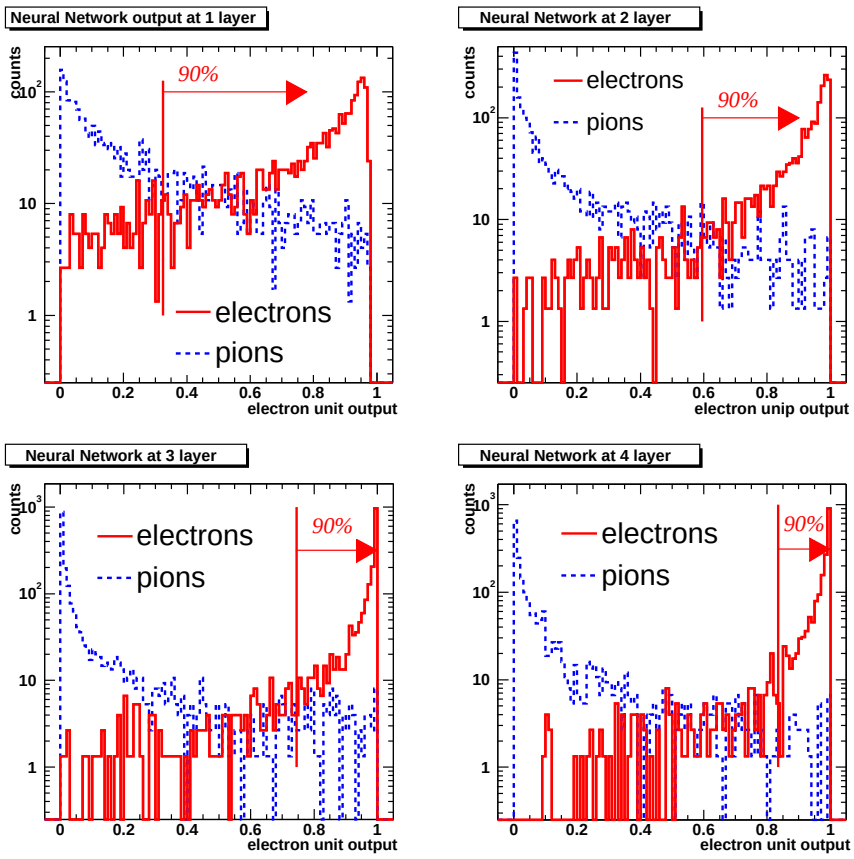

Figure 4.24: The output distributions of electron excite unit for test data. Upper left figure is the distribution for 1 TRD layer. Upper right figure is the distribution for 2 TRD layers. Lower left figure is the distribution for 3 TRD layers. Lower right is for 4 TRD layers

After extrapolating to 6 TRD layers as shown in Fig. 4.25, the pion misidentification probability at 90% electron efficiency achieves to be 0.32%, which corresponds to pion rejection factor of 313. The momentum dependence of pion rejection factor based on neural network is shown in Fig. 4.26. For comparison with the 2DLQ likelihood method, the probability distribution function were extracted from the learning data. Then the likelihood ratio was evaluated for the test data set and pion rejection factor was extracted. The results based on 2DLQ method are also shown in Fig. 4.26 and the comparison of pion rejection factor between neural network and 2DLQ method is summarized in Table 4.8. Pion rejection factor is slightly

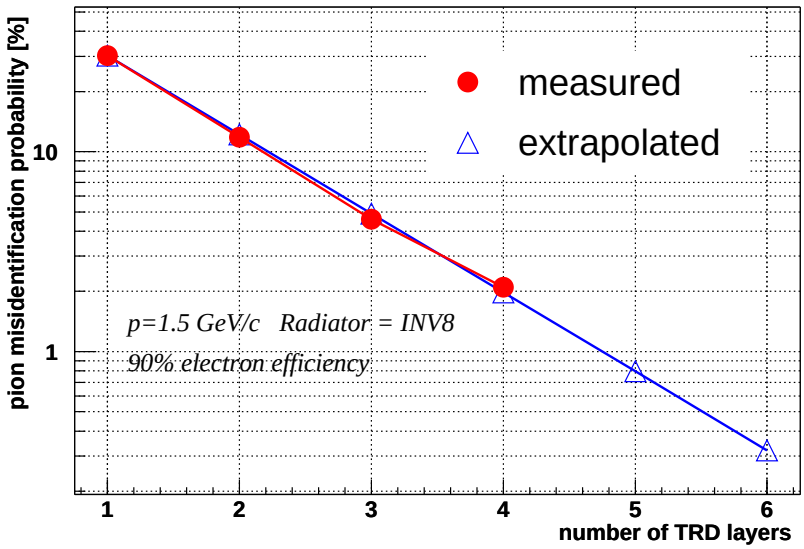

Figure 4.25: Pion misidentification probability as a function of number of TRD layers. Circle means the measured value and triangle means the extrapolated value.

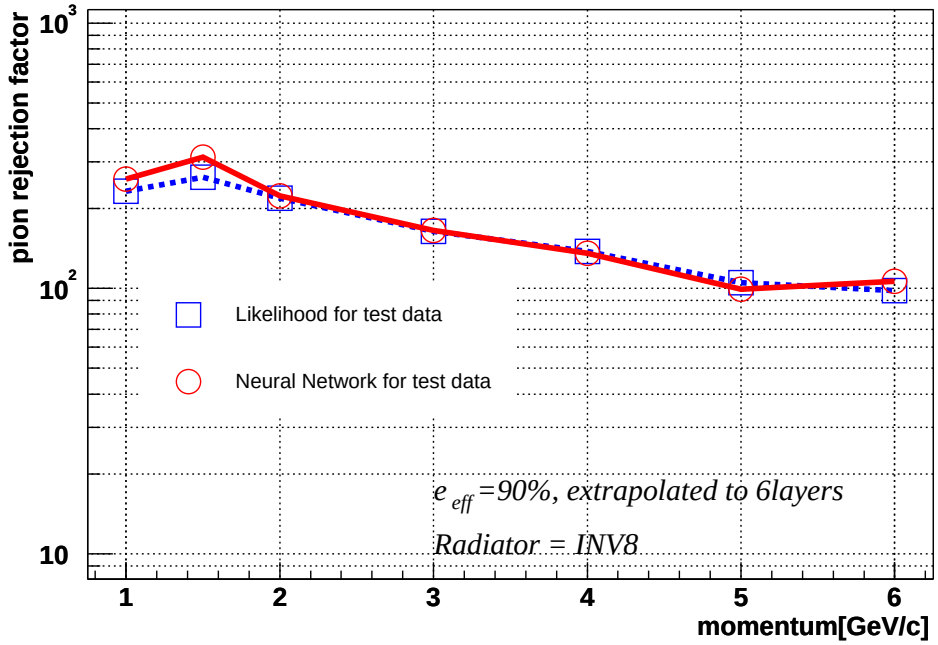

Figure 4.26: Pion rejection factor based on neural network as a function of beam momentum.

Table 4.8: Comparison of pion rejection factor based on neural network and 2DLQ method.

Method	1 GeV/c	1.5 GeV/c	2 GeV/c	3 GeV/c	4 GeV/c	5 GeV/c	6 GeV/c
Neural Network	258.3	312.5	223.1	165.6	135.5	99.4	106.5
2DLQ	232.6	263.2	219.3	164.2	137.7	105.3	98.0

improved by a neural network for momenta below 2 GeV/c and almost the same for momenta above 3 GeV/c. This indicates that the neural network can be a good analysis method for the electron identification using the TRD.

Figure 4.27 shows the energy deposit distribution of electrons (red line) and pions (blue line) in each drift region. The particle momentum is 2 GeV/c. The energy deposit distributions of the pion events whose output value of electron excite unit is more than 0.9 are also shown in the shaded area. It is seen from the figure that some of the misidentified pions look like electrons with rather high energy deposit. These misidentified pions have a close relation to the production of δ electrons in the drift chamber [32].

Electrons ejected with an energy greater than a few keV are normally called δ electrons. The expression of the probability for an electron to receive the energy E per unit length is approximately given by the following equation [33]:

$$P(E) = K\frac{Z}{A}\frac{\rho}{\beta^2}\frac{1}{E^2} = \frac{W}{E^2} \tag{4.25}$$

where $K = \frac{2\pi N z^2 e^4}{mc^2}$, N is the Avogadro number, m and e are the electron mass and charge, Z, A and ρ are the atomic number, mass and the density of medium, respectively and X is the length of particle trajectory. The number of electrons liberated per unit length and having the energy more than E_0 is obtained by integrating Eq. 4.25:

$$\frac{dN(E \geq E_0)}{dX} = \int_{E_0}^{E_M} P(E)dE = W\Big(\frac{1}{E_0} - \frac{1}{E_M}\Big) \tag{4.26}$$

where E_M is the maximum energy transfer and has following relations:

$$E_M = \frac{2mc^2\beta^2}{1-\beta^2} \tag{4.27}$$

Figure 4.28 shows the integrating number of electrons liberated per unit length with the energy greater than E. Solid line is the result simulated by GEANT3 [35] and dashed line is the result extracted by Eq. 4.26. The lowest energy in Fig. 4.28 corresponds to the ionization potential of Xe ($I = 12.13$ eV), while the ionization potential of CO_2 is $I = 13.81$ eV.

The range which ejected electrons will cover is expressed as follows [32]:

$$R(E) = AE\Big(1 - \frac{B}{1+CE}\Big) \tag{4.28}$$

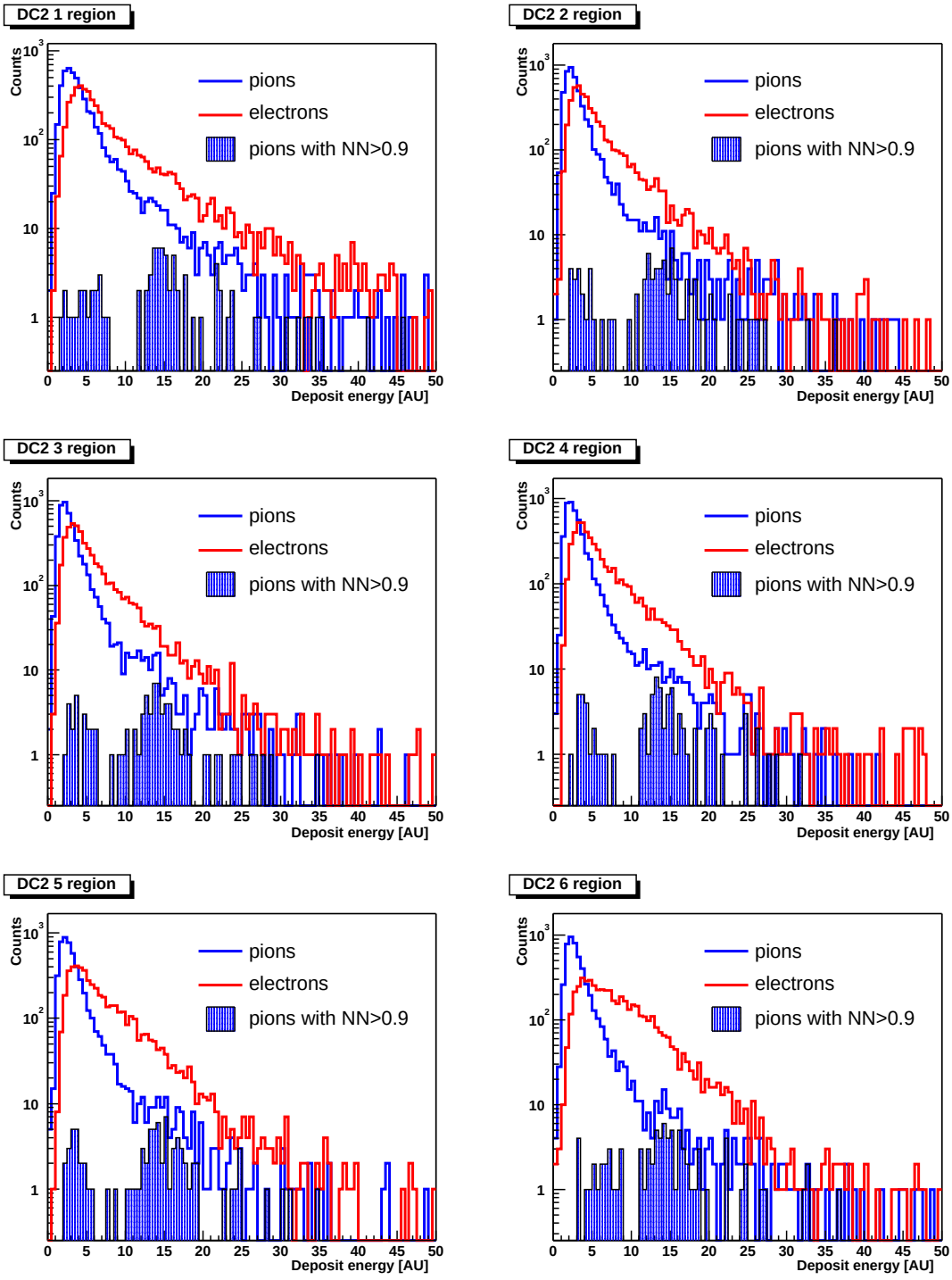

Figure 4.27: The energy deposit distributions of each drift region. Shaded areas are the spectra of misidentified pions, red lines and blue lines are electron spectra and pion spectra, respectively. The beam momentum is 2 GeV/c.

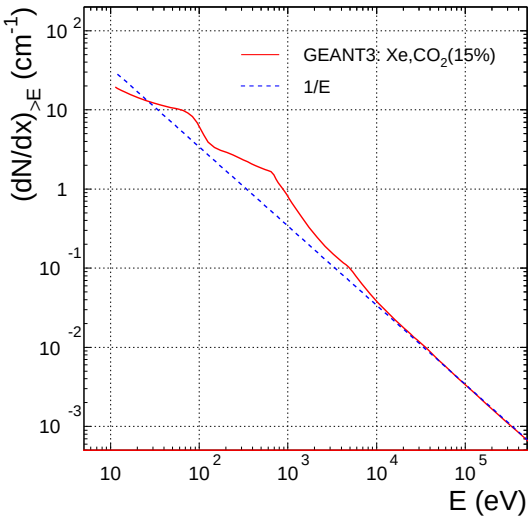

Figure 4.28: The number of electrons liberated per unit cm with the energy more than E in Xe gas [32].

where $A = 5.37 \times 10^{-4}$ gcm^{-2}keV^{-1}, $B = 0.9815$ and $C = 3.123 \times 10^{-3}$ keV^{-1}. E is the energy of δ electron. For instance, the range is 0.52 mm for 10 keV and is 27.4 mm for 100 keV δ electrons. If the δ electron is produced such that the range in Eq. 4.28 is greater than the detector depth, it escapes from the detector and is treated as an additional track to the parent track.

Figure 4.29 shows the energy loss spectrum for pions with momentum of 2 GeV/c for all tracks, for tracks not containing any δ electrons, for tracks with δ electrons which are absorbed in the detector and for tracks with δ electrons for which one δ electron escapes from the detector. It is noticed that the long tail originates from the contribution of δ electrons. 15.3% of all tracks have δ electrons with energy greater than 10 keV and 16.3% of them, which corresponds to 2.5% of all tracks, escape from the TRD. Figure 4.30 shows the real data of energy deposit taken for pion momentum of 2 GeV/c, where this figure is scaled such that the peak position is the same as that of Fig. 4.29. Almost the same shape is seen when compared Fig. 4.30 to Fig. 4.29. This implies that the δ electrons contribute the long tail of energy deposit spectrum and that some misidentified pions contains δ electrons.

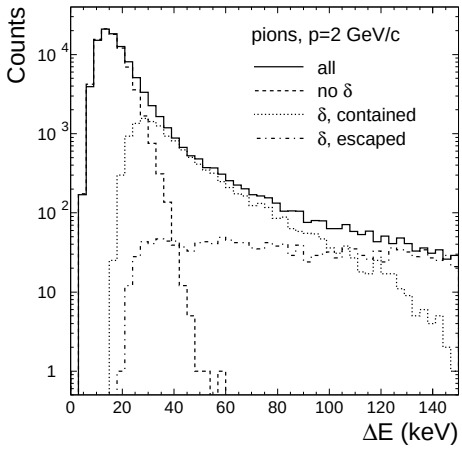

Figure 4.29: Simulated energy loss of 2 GeV/c pions in the TRD. Solid line is the energy loss for all tracks, dashed line is that for the tracks which do not have any δ electrons, dotted line is that for tracks with δ electrons which do not escape from the detector and dot-dashed line is that for tracks which δ electrons escape from the detector.

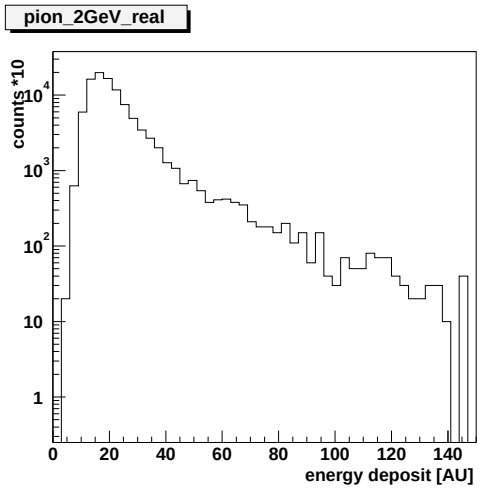

Figure 4.30: Read data of energy loss of 2 GeV/c pions in the TRD.

4.7 Incident angle dependence

To evaluate the incident angle dependence of pion rejection, the measurements were performed with the incident angle of 0, 5, 10 and 15 degrees. The INV6 radiator was used and the beam momentum was 3 GeV/c in these measurements.

Figure 4.31 shows the average pulse height distributions for electrons (left) and pions (right) as a function of drift time for different incident angles. Figure 4.32 shows the ratios of mean

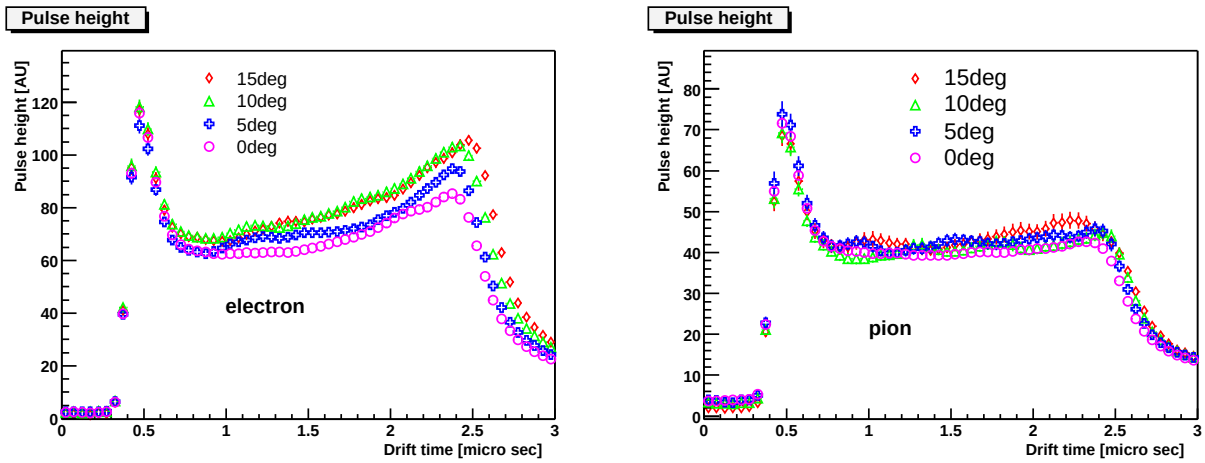

Figure 4.31: Average pulse height as a function of drift time, for different incident angles. Left panel: electrons, right panel: pions.

pulse heights of electrons to those of pions as a function of drift region (left panel), the ratios of mean pulse heights of electrons to those of electrons at 0 deg (central panel) and the ratios of mean pulse heights of pions to those of pions at 0 deg. The drift region is defined as Table 3.3.

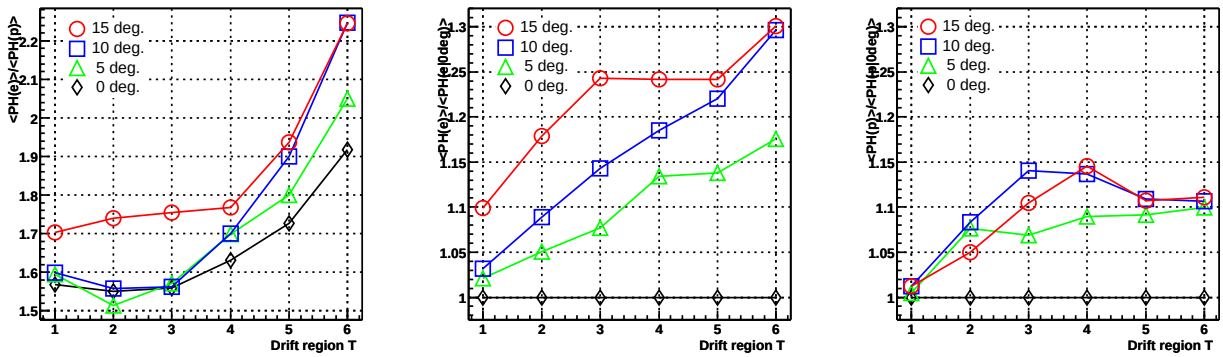

Figure 4.32: Left panel: Average pulse heights ratios as a function of drift region. Central panel: Average pulse heights ratios of electrons to those of electrons at 0 deg. Right panel: Average pulse heights ratios of pions to those of pions at 0 deg.

From Fig. 4.31 and Fig. 4.32, the pulse heights for electrons and pions decrease and signal is attenuated as a function of drift time, which can be seen more clearly in case of electrons than pions, as the incident angle decreases towards 0°. The separation of energy deposit spectra between electrons and pions is more difficult as incident angle becomes smaller since the ratio of mean pulse heights of electrons to those of pions becomes smaller as shown in the left panel of Fig. 4.32.

There are two possible reasons that the pulse heights decrease as the incident angle becomes smaller. One is the influence of shorter track length. The other is the influence of space charge effect due to the slow movement of positive ions created in the avalanche [33, 34]. This space charge effect leads to a local gain reduction.

The detector depth $X(\theta)$ for different incident angle θ is expressed as $X(\theta) = X(0)/\cos\theta$, where X_0 is the detector depth for nominal incidence and equals to 3.7 cm. The detector depth becomes about 3.83 cm, 3.75 cm and 3.72 cm for incident angle of 15°, 10° and 5°, respectively. Assuming that the reason of the degradation of pulse heights is due to the less energy deposit as a result of shorter track length, the attenuation of the pulse heights would not depend on the drift time. The different tendency from this expectation can be seen and this reason is thought to be due to space charge effect.

Since it takes a few μs for the positive ions to move away from the anode surface to a distance of several tens of wire radius, the gain reduction due to space charge is existed during the drift time of 2 μs. The signal in amplification region is independent of incident angle, since there doesn't exist previous avalanches and the contributions of the difference of track length is thought to be negligible. The space charge effect can be seen around the end of drift time. As shown in Fig. 4.31 and Fig. 4.32, the degradation of pulse heights are larger at later drift time, while the pulse heights at avalanche region are almost the same for different incident angles. It is noted form Fig. 4.31 and Fig. 4.32, the electrons suffer a stronger signal attenuation than pions. This is due to the larger signals of electrons derived from larger energy deposit than that of pions. The gain reduction due to the space charge effect depends on the potential of anode wires [34]. In this situation, where the potential of anode wire is 1.5 kV, the gain reduction occurs in case of incident angle below 10° as shown in Fig. 4.31.

Since the degradation of pulse heights at smaller incident angle due to space charge effect can be seen and signal attenuation is stronger for electrons, pion rejection are expected to be worse as incident angle becomes smaller.

The pion rejection factor was analyzed by 2DLQ method since two data sets is needed to apply neural network method and this leads to less statistics to extract pion rejection factor.

The pion rejection factor as a function of incident angle is shown in Fig. 4.33. The better pion rejection factor is achieved when the incident angle of charged particle becomes larger. The degradation of pion rejection at smaller incident angle is due to space charge effect as described above. Though the pion rejection is the worst at incident angle of 0°, the pion rejection factor is within requirement of the ALICE TRD.

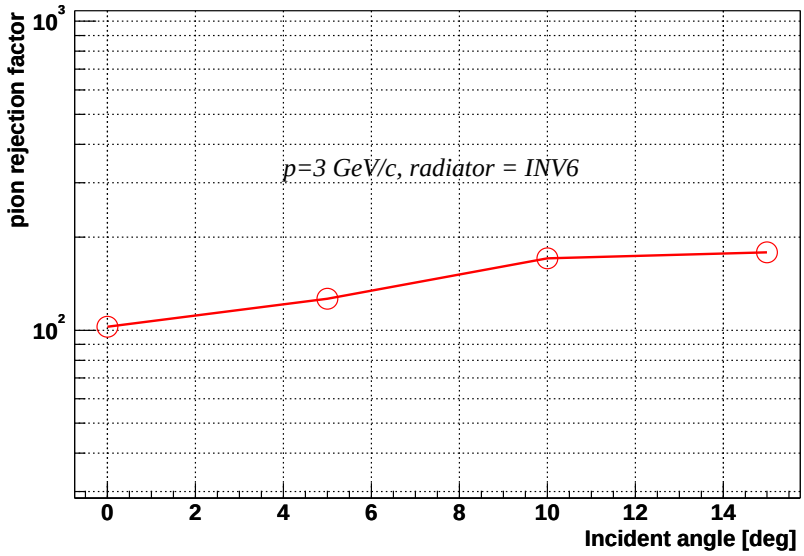

Figure 4.33: Pion rejection factor as a function of incident angle. Radiator is INV6 and beam momentum is 3 GeV/c.

4.8 Magnetic field dependence

Since the ALICE TRD will be installed in the L3 magnet (B=0.4 T), the magnetic field dependence of pion rejection is a very important issue. The measurements were performed in case of magnetic field of 0 T, ±0.14 T, ±0.28 T, ±0.42 T and ±0.56 T. The beam momentum was 6 GeV/c, incident angle is 0° and INV6 radiator was used. Because the trigger reduction of pion events wasn't performed, the number of electron events ($\sim$ 400) were too small compared with that of pions ($\sim$ 15000) as shown in Table. 4.4. Therefore it was difficult to apply the likelihood method because the probability distributions had large ambiguity in statistics for electron events. In this analysis, the neural network was used but because of low statistics of electron events, the connection weights were fixed to be the same as those for the beam momentum of 6 GeV/c, incident angle of 15°, radiator of INV6 and magnetic filed of 0 T. Figure 4.34 shows the pulse heights distributions for electrons (left) and pions (right) as a function of drift time for different magnetic fields. The ratios of mean pulse heights of electrons to those of pions as a function of drift region is shown in Fig. 4.35, where the definition of drift region is the same as Table. 3.3.

When the magnetic field exists, the drift electrons move at an angle with respect to the lines of electric field. This angle is called Lorentz angle, Ψ_L, and it can be expressed as follows:

$$\tan \Psi_L = \omega\tau \tag{4.29}$$

where ω is the cyclotron frequency and τ is the mean time interval between two collisions of electrons in the gas. The drift velocity also changes due to the magnetic field as follows:

$$v_D = \frac{v_D(B=0)}{\sqrt{1+\omega^2\tau^2}} \tag{4.30}$$

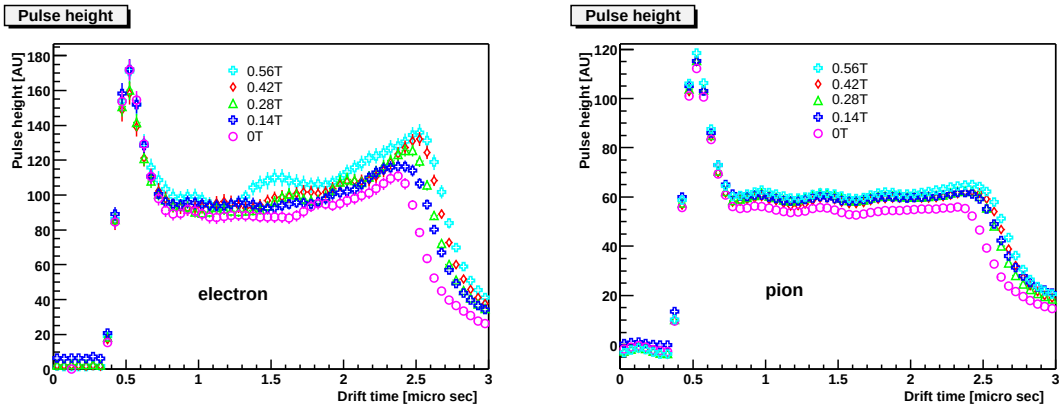

Figure 4.34: Pulse heights distributions for electrons (left) and pions (right) as a function of drift time for different magnetic fields

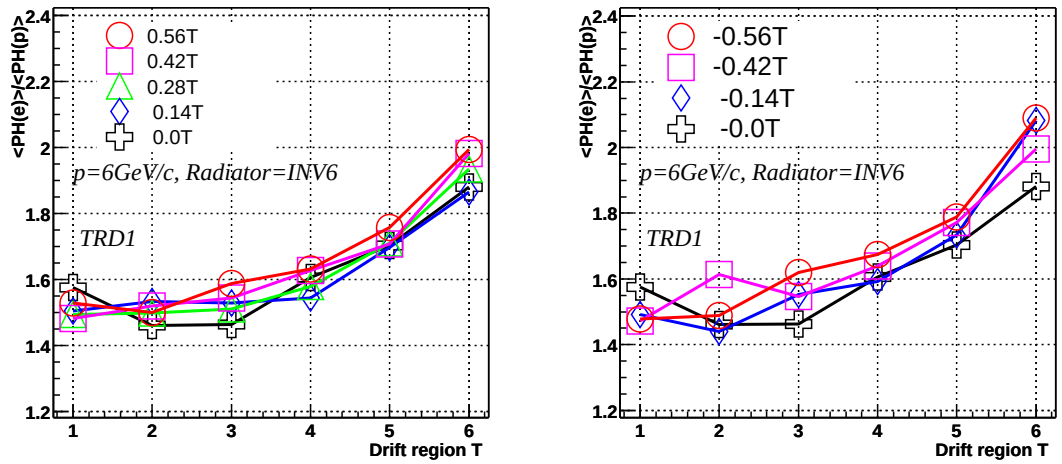

Figure 4.35: Average relative electron/pion pulse heights as a function of drift region for various magnetic fields. Radiator is INV6 and beam momentum is 6 GeV/c.

The derivation of Eq. 4.29 is summarized in Appendix B.

Since Lorentz angle becomes 8° in case of magnetic filed of 0.4 T [3], electric field of 0.7 kV/cm and gas composition of Xe(85%)/CO_2(15%), the Lorentz angle for magnetic field of 0 T, 0.14 T, 0.28 T, 0.42 T and 0.56 T can be obtained under the same condition and is summarized in Table 4.9.

Table 4.9: Lorentz angle for different magnetic fields of the test experiment.

Magnetic field [T]	Lorentz angle [degree]
0.56	11.13
0.42	8.4
0.28	5.6
0.14	2.8
0.0	0.0

When the magnetic field exists, two possible influences on pion rejection must be considered. One is the space charge effect due to Lorentz angle of drift electrons. Since the Lorentz angle varies from 0° to 11.13°, space charge effect is expected to be appeared as described in the previous section. The other is the less contribution of the δ electrons because δ electrons curl up in the magnetic field.

From Fig. 4.34, drift time dependence of signal attenuation due to the space charge effect can be seen. Moreover the drift velocity decreases as the magnetic field becomes larger as demonstrated in Eq. 4.30. The space charge affects the pulse heights of pions but the signal attenuation cannot be seen from Fig. 4.34. When magnetic field becomes larger, the pulse heights are expected to be higher compared to those in case of smaller magnetic field but since the δ electrons curl up in the magnetic field and they are spatially separated from pion track, this effect leads to the degradation of the pulse heights of pions. Because of these two effects, the pulse heights of pions are almost the same for magnetic field above 0.14 T.

The average pulse height ratio as shown in Fig. 4.35 is larger as the magnetic filed becomes larger. The better separation of energy deposit spectra between electrons and pions is possible as magnetic field becomes larger since the ratio of mean pulse heights of electrons to those of pions becomes larger. Therefore it is expected that the pion rejection is improved as magnetic field becomes larger.

The pion rejection factor was extracted by the neural network and its magnetic field dependence is shown in Fig. 4.36.

Since the pion rejection factor is the worst in case of beam momentum of 6 GeV/c and incident angle of 0 degree and the connection weights haven't been optimized yet, the pion rejection factor is below 100 for all magnetic fields. However, it is noted that the pion rejection factor is improved when the magnetic field is on compared to result in case of magnetic field off. This dependence is derived from less contribution of δ electrons and less space charge effect of electron tracks as the magnetic field becomes larger.

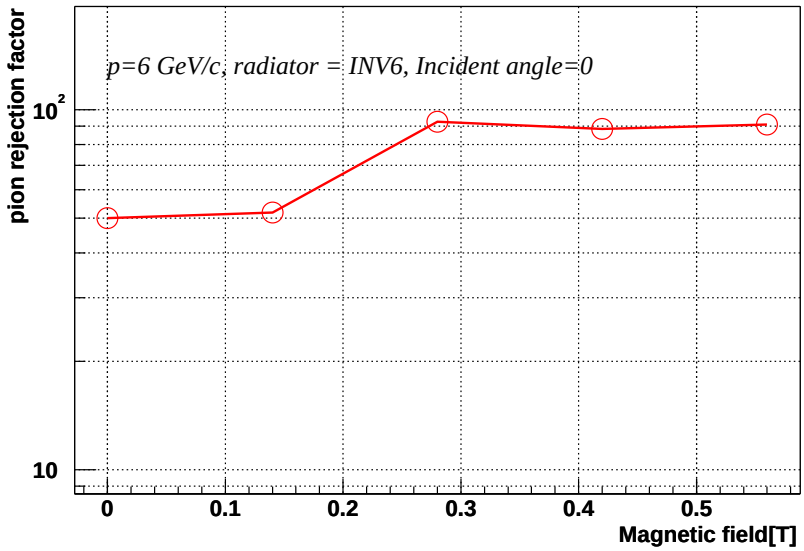

Figure 4.36: Pion rejection factor as a function of magnetic field.

Chapter 5

Conclusion

ALICE TRD has important roles such as electron identification by detecting transition radiation and particle tracking via energy loss of charged particles. In this thesis, electron identification capability was discussed including the traditional and new analysis methods.

Prototype TRD can respond to electrons and pions as it is expected. For electrons, the contribution of the transition radiation can be seen clearly in energy deposit spectrum and drift time dependence of the measured pulse heights.

The pion rejection factor was studied by different analysis methods. Likelihood ratio method provides pion rejection factor above 100 for beam momentum up to 6 GeV/c by using the drift time dependence of pulse heights. This satisfies the requirement of the ALICE TRD and demonstrates that Likelihood method is useful analysis method of electron identification.

Neural network method, which is a new analysis method, was used to study pion rejection performance. It was demonstrated that the neural network is able to find the enhancement of pulse heights around the end of drift time spontaneously and identify the electrons sufficiently by judging the enhancement of pulse heights, which is the expectation to neural network. The pion rejection reached to be more than 300 in case of beam momentum of 1.5 GeV/c and more than 100 for all momenta. The best pion rejection was achieved by neural network. This indicates that neural network can be applied to the study of electron identification.

There are no critical problems in pion rejection for all sandwiched radiators and pion rejection satisfies the design goal of the final ALICE TRD for them. From the momentum dependence of pion rejection, electron identification capability becomes worse as momentum becomes larger. This is because the energy loss of pions is larger as momentum becomes larger, while the electron energy loss and TR yield is constant for all momenta. However, the ALICE TRD will install in L3 magnet and the magnetic field dependence of pion rejection shows that electron identification capability is improved as larger magnetic field due to the less contribution of δ electrons and space charge effect.

The results of incident angle dependence of pion rejection shows the electron identification capability is within requirement for all azimuthal incident angles. However, the degradation of pion rejection is seen as incident angle becomes smaller. This is due to the space charge effect. To minimize the space charge effect, the gas gain must be as low as possible.

Acknowledgment

I'm most grateful to Prof. H. Hamagaki. His abundant knowledge and his many pieces of advice helped me to study the electron identification capability of the ALICE TRD.

I thank Dr. Anton Andronic who is the leader of the ALICE TRD team. Without his introduction, I would not have myself a time at the ALICE TRD and could not get many pieces of knowledge about transition radiation. Moreover I thank him for his help in the data analysis and a great deal of valuable advice. I appreciate Dr. K. Ozawa and Dr. M. Inuzuka. Without discussions with them, I could not carry out my study. I'm also grateful to Dr. K. Oyama and Dr. B. Vulpescu for their advise and many valuable comments on my analysis.

I wish to acknowledge all the members of the ALICE TRD team. My work would never be completed without their efforts at constructing prototype TRD and at constructing analysis tools.

Appendix A

Theoretical description of Transition Radiation

Transition Radiation is the electromagnetic radiation that is emitted when a charged particle with relativistically high momentum transverses the boundary between two media with different dielectric constants ϵ_1 and ϵ_2. Transition Radiation is the result of the reformation of the particle's field when a particle passes from a medium with ϵ_1 to a medium with ϵ_2. In this chapter, the important theoretical results [9, 10, 11] are summarized.

A.1 Single interface

The double differential energy spectrum emitted when a charged particle with Lorentz factor γ passes a boundary between two media with different dielectric constants (ϵ_1 and ϵ_2) is written as the following expression:

$$\Big(\frac{\mathrm{d}^2\mathrm{W}}{\mathrm{d}\omega\mathrm{d}\Omega}\Big)_{interface} = \frac{\alpha}{\pi}\Big(\frac{\theta}{1/\gamma^2+\theta^2+\omega_1^2/\omega^2} - \frac{\theta}{1/\gamma^2+\theta^2+\omega_2^2/\omega^2}\Big)^2 \tag{A.1}$$

where ω_1 and ω_2 are the plasma frequency of the two media, θ is the emission angle of the photon with respect to the particle trajectory and α is the fine structure constant. The plasma frequency is a material property and has the following relation:

$$\omega_{1,2} = \sqrt{\frac{4\pi\alpha n_{1,2}^e}{m_e}} = 28.8\sqrt{\rho\frac{Z}{A}} \quad \mathrm{eV} \tag{A.2}$$

where n^e and m_e are the electron density and mass.

The differential energy spectrum is obtained by integrating Eq. A.1 over the solid angle and is described as follows:

$$\Big(\frac{\mathrm{dW}}{\mathrm{d}\omega}\Big)_{interface} = \frac{\alpha}{\pi}\Big(\frac{\omega_1^2+\omega_2^2+2\omega^2/\gamma^2}{\omega_1^2-\omega_2^2}\ln\frac{1/\gamma^2+\omega_1^2/\omega^2}{1/\gamma^2-\omega_2^2/\omega^2} - 2\Big) \tag{A.3}$$

The total intensity of TR emitted at a single interface is described as follows:

$$\mathrm{W}_{interface} = \frac{\alpha}{\pi}\frac{(\omega_1-\omega_2)^2}{\omega_1+\omega_2}\gamma \tag{A.4}$$

From these equations, some remarkable features of TR are summarized as follows:

- The total intensity of TR increases in proportional to the Lorentz factor of the charged particle.
- The emission angle of TR is $\sim 1/\gamma$. The effect is peaked in the forward direction.
- The probability of creating a photon is of the order of α.
- Most of the radiation is emitted in X-ray region for highly relativistic particles.

A.2 Multiple interface

Since the probability of emission of photons per boundary is small ($\simeq 10^{-2}$), it is necessary to prepare multiple interfaces for the effective creation of TR photons. When a stack of N_f foils of thickness l_1 is separated by a medium (usually a gas) of thickness l_2, the double differential energy spectrum per one foil is described as follows by summing up the contributions of two interfaces:

$$\Big(\frac{\mathrm{d}^2\mathrm{W}}{\mathrm{d}\omega\mathrm{d}\Omega}\Big)_{foil} = \Big(\frac{\mathrm{d}^2\mathrm{W}}{\mathrm{d}\omega\mathrm{d}\Omega}\Big)_{interface} \times 4\sin^2(\phi_1/2) \tag{A.5}$$

where $4\sin^2(\phi_1/2)$ is the interface factor and ϕ_1 is the phase retardation in one foil and described as the following relation:

$$\phi_1 \simeq (\gamma^{-2} + \theta^2 + \omega_1^2/\omega^2)\omega l_1/2 = 2 \times \Big(\frac{l_1}{Z_1}\Big) \tag{A.6}$$

The "formation zone "for the foil medium, Z_1, is introduced from Eq. A.6.

$$Z_1 \equiv \frac{4}{\omega}\Big(\frac{1}{\gamma^2} + \theta^2 + \frac{\omega_1^2}{\omega^2}\Big)^{-1} \tag{A.7}$$

For a stack of N_f foils, the double differential energy spectrum is described as follow:

$$\Big(\frac{\mathrm{d}^2\mathrm{W}}{\mathrm{d}\omega\mathrm{d}\Omega}\Big)_{stack} = \Big(\frac{\mathrm{d}^2\mathrm{W}}{\mathrm{d}\omega\mathrm{d}\Omega}\Big)_{foil} \times \exp\Big(\frac{1-N_f}{2}\sigma\Big)\frac{\sin^2(N_f\phi_{12}/2) + \sinh^2(N_f\sigma/4)}{\sin^2(\phi_{12}/2) + \sinh^2(\sigma/4)} \tag{A.8}$$

where $\phi_{12} = \phi_1 + \phi_2$ is the phase retardation and $\sigma = \sigma_1 + \sigma_2$ is the total absorption cross section for the radiator (foil + space). From ϕ_2, the "formation zone " for this medium can be defined in the same way as Eq. A.6 and Eq. A.7.

From these equations, TR produced by a multilayered radiator can be characterize as follows:

- The yield is suppressed if $l_i \ll Z_i$. This is what is called "formation zone effect".
- The multiple foil interface governs the saturation of the TR yield at high γ, above the value:

$$\gamma_s = \frac{1}{4\pi}\Big[(l_1 + l_2)\omega_1 + \frac{1}{\omega_1}(l_1\omega_1^2 + l_2\omega_2^2)\Big] \tag{A.9}$$

- The TR spectrum has the most relevant maximum at $\omega_{max} = l_1\omega_1^2/2\pi$. This allows the tuning of TRD by varying the material and the thickness of the radiator foils.

Appendix B

Drift electrons in the Magnetic field

The equation of motion for electrons with velocity $\vec{v}$ can be expressed as follows when the electric field $\vec{E}$ and magnetic field $\vec{B}$ exist:

$$m\dot{\vec{v}} = -e(\vec{E} + \vec{v} \times \vec{B}) + m\vec{A}(t) \tag{B.1}$$

where m is the electron mass and $\vec{A}(t)$ is the fluctuating force. This equation is known as the Langevin equation and time average can be applied. Since the solution of Eq. B.1 is the translation with the constant velocity $\vec{v}_D$, the left hand side of Eq. B.1 must vanish. Hence, the fluctuating force is expressed as follows:

$$< \vec{A}(t) >= -\frac{\vec{v}_D}{\tau} \tag{B.2}$$

where τ is the mean time interval between two collisions of electrons. Then Eq. B.1 can be expressed as follows:

$$\dot{\vec{v}}_D = -\frac{e\vec{E}}{m} - \frac{e\vec{v} \times \vec{B}}{m} - \frac{\vec{v}_D}{m} \tag{B.3}$$

Since $\dot{\vec{v}}_D = 0$ for constant $\vec{E}$, Eq. B.3 can be written as follows:

$$\frac{e\vec{E}}{m} = -\frac{e\vec{v} \times \vec{B}}{m} - \frac{\vec{v}_D}{m} \tag{B.4}$$

The solution of $\vec{v}_D$ can be obtained as follows:

$$\vec{v}_D = \frac{-\mu}{1 + \omega^2\tau^2}\Big(\vec{E} + \frac{\vec{E} \times \vec{B}}{B}\omega\tau + \frac{(\vec{E} \cdot \vec{B})\vec{B}}{B^2}\omega^2\tau^2\Big) \tag{B.5}$$

where $\mu = e\tau/m$ is the electron mobility and $\omega = eB/m$ is the cyclotron frequency.

In case of the magnetic field perpendicular to the electric field, drift velocity has a component $\vec{v}_{D\perp}$ in direction of $\vec{E} \times \vec{B}$ and a component $\vec{v}_{D\parallel}$ in direction of $\vec{E}$. They are expressed as follows:

$$v_{D\perp} = \mu E \frac{\omega\tau}{1 + \omega^2\tau^2} \tag{B.6}$$

$$v_{D\parallel} = -\mu E \frac{1}{1 + \omega^2\tau^2} \tag{B.7}$$

From two components, the magnitude of the drift velocity is obtained:

$$v_D = \mu E \frac{1}{\sqrt{1+\omega^2\tau^2}} \tag{B.8}$$

The angle between $\vec{v}_D$ and $\vec{E}$, the Lorentz angle, is

$$\tan \Psi_L = \omega\tau \tag{B.9}$$

Figure B.1 shows the drift path of electrons without magnetic field (left) and with magnetic field (right).

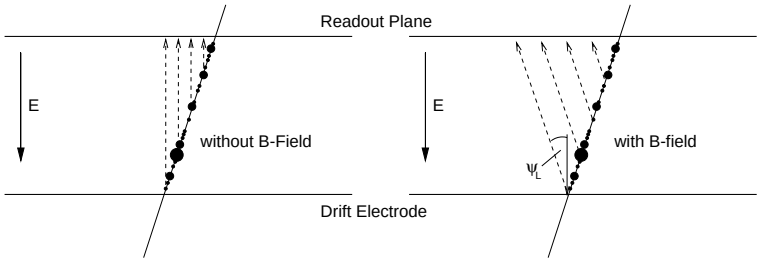

Figure B.1: The drift path of electrons without magnetic field (left) and with magnetic field (right).

Bibliography

[1] ALICE Collaboration Technical Proposal CERN/LHCC/95-97

[2] J.W. Harris and B. Müller hep-ph/9602235

[3] ALICE TRD Technical Design Report, CERN/LHCC, Octorber 2001; http://www.gsi.de/˜alice/trdtdr

[4] ALICE Collaborarion, A Transition Radiation Detector, Technical Proposal, Addendum 2, CERN/LHCC/99-13

[5] T. Matsui and H. Satz, Phys. Lett. B **178**, (1986) 416

[6] A. Andronic *et al.*, [nucle-th/0303036]

[7] R. L. Thews *et al.*, Phys. Rev. C **63** (2001) 054905

[8] V.L. Ginzburg and I.M. Frank, Zh. Eskp. Theor. Fiz. **16** (1946) 15

[9] M.L. Cherry *et al.*, Phys. Rev. D **10**, 3594 (1974)

[10] X. Artru *et al.*, Phys. Rev. D **12**, 1289 (1975)

[11] L. Durand, Phys. Rev. D **11**, 89 (1975)

[12] B. Dolgoshein, Nucl. Instr. Meth **A 326** (1993) 434

[13] V. Egorytchev *et al.*, Nucl. Instr. Meth **A 453** (2000) 346

[14] M.L. Cherry *et al*, Nucl. Instr. Meth **115** (1974) 141

[15] G.B. Bassompierre *et al*, Nucl. Instr. Meth **411** (1998) 63

[16] R.D Appuhn *et al*, Nucl. Instr. Meth **263** (1988) 309

[17] E.O'Brien *et al*, IEEE Trans. Nucl. Sc. **40** 153 (1993)

[18] T. Akesson *et al*, Nucl. Instr. Meth **A 372** (1996) 70

[19] A. Andonic *et al.*, IEEE Trans. Nucl. Sc. vol **48** 1259 (2001) [nucl-ex/0102017]

[20] A. Andonic *et al.*, Nucl. Instr. Meth. **A 498** (2003) 143-154

[21] H.G. Essel and N. Kurz, IEEE Trans.Nucl.Sci **47** (2000) 337.

[22] RIO2 VME Power PC http://www.ces.ch/

[23] http://psdata.web.cern.ch/psdata/www/eastareaop/

[24] A. Bungener *et al*, Nucl. Instr. Meth. **A 214** (1983) 261-168

[25] Enrique Garcia-Berro *et al*, Neural Network **16** (2003) 405

[26] C. Peterson *et al*, Comput. Phys. Commun **81** (1994) 185

[27] L. Lonnblad *et al*, Phys. Rev. Lett **65** (1990) 1321

[28] L. Lonnblad *et al*, Comput. Phys. Commun **67** (1991) 193

[29] G. Stimpfl-Abele *et al*, Comput. Phys. Commun **78** (1993) 1

[30] W. S. Babbage *et al*, Nucl. Instr. Meth **A 330**(1993)482

[31] A. N. Kolmogorov, Dokl. Akad. Nauk. USSR 114 (1957) 935

[32] A. Andronic *et al*, [physics/0310122]

[33] F. Sauli, CERN Report 77-09 (1977)

[34] A. Andronic *et al*, *submitted to the Nucl. Instr. Meth* **A**

[35] GEANT 3.21 Package, CERN Program Library W5013